Title

Telencephalic outputs from the medial entorhinal cortex are copied directly to the hippocampus

Authors and Affiliations

Sau Yee Tsoi, Merve Öncül, Ella Svahn, Mark Robertson, Zuzanna Bogdanowicz, Christina McClure and Gülşen Sürmeli*

*Corresponding Author

University of Edinburgh, Centre for Discovery Brain Sciences, Edinburgh, UK:
G.S., S.Y.T., M.Ö., E.S., M.R., Z.B., C.M.

Simons Initiative for the Developing Brain:
G.S.

Current addresses

University College London, UK:
E.S.

NHS Greater Glasgow and Clyde, UK:
M.R.

VectorBuilder Inc., 1010 W 35th Street, Suite 515 Chicago, IL 60609, USA:
C.M.

Abstract

Complementary actions of the neocortex and the hippocampus enable encoding and long-term storage of experience dependent memories. Standard models for memory storage assume that sensory signals reach the hippocampus from superficial layers of the entorhinal cortex (EC). Deep layers of the EC on the other hand relay hippocampal outputs to the telencephalic structures including many parts of the neocortex. Here we show that cells in Layer 5a of the medial EC send a copy of their telencephalic outputs back to the CA1 region of the hippocampus. Combining cell-type specific anatomical tracing, high-throughput RNA-sequencing based projection mapping and optogenetics aided circuit mapping, we show that these projections have a unique topography and target hippocampal pyramidal cells and interneurons. Our results suggest that rather than serving as a relay, deep EC may coordinate hippocampal-neocortical interactions in spatial cognition and memory.

Introduction

Interplay between the hippocampus and the neocortex is a central tenet of theories for systems memory consolidation (Marr, 1971; McClelland et al., 1995). The entorhinal cortex (EC) mediates the two-way communication between the neocortex and the hippocampus. Its superficial and deep layers respectively channel inputs to and outputs from the hippocampus. During a new experience the superficial layers relay convergent inputs from the cortex to the hippocampus where initial conjunctive representations of everyday experiences are generated. Subsequently during rest or sleep, hippocampal output is redistributed to the brain (Squire et al., 2015; Frankland and Bontempi 2005). Leading theoretical models consider the deep layers of EC as a relay of hippocampal output that reinstates neocortical activation patterns representing memories, enabling neocortex-wide synaptic changes required for long-term storage (Koster et al., 2018; Kumaran et al., 2016; McClelland et al., 1995; Schapiro et al., 2017).

Recent discoveries revealed complex and distinct input-output interactions of molecularly defined subtypes of neurons in the deep layers of medial EC (MEC), suggesting their functions extend beyond passing on hippocampal outputs. Layers 5a (L5a) and 5b (L5b) of the EC are genetically distinct with differential input-output organisations. L5a but not L5b is the sole origin of the long-range telencephalic outputs of the EC (Sürmeli et al., 2015), whereas L5b, but not L5a, is directly influenced by superficial layers of EC (Beed et al., 2020; Sürmeli et al., 2015). Inputs from the dorsal hippocampus preferentially target L5b over L5a (Rozov et al., 2020; Sürmeli et al., 2015; Wozny et al., 2018) whereas ventral hippocampus preferentially target L5a (Rozov et al. 2020). Moreover, the capacity of deep layers to integrate neocortical inputs with hippocampal output (Czajkowski et al. 2013; Beed et al. 2020; Sürmeli et al. 2015), suggest more complex roles.

An intriguing possibility, noted in experiments with classic retrograde tracers, is that deep layers of MEC might also project to the hippocampal CA1 region, which provides the deep EC with hippocampal output (Köhler, 1985; Witter and Amaral, 1991). Such recurrent connectivity between CA1 and the deep MEC could be important in coordinating hippocampal-entorhinal activity during memory consolidation (Ólafsdóttir et al. 2016), provide a shortcut for hippocampal outputs to re-enter the hippocampus (Kumaran and McClelland 2012) or have a more global coordination function encompassing the hippocampus and the neocortex (Khodagholy et al., 2017). Despite its potential functional significance, the key properties of this projection pathway including whether it shares the same source with the telencephalon projections and which neurons it targets in the hippocampus remain unknown.

Here we reveal that, neurons in L5a, but not L5b, of the MEC project to hippocampal CA1. We establish that the telencephalon-projecting neurons copy their outputs directly to pyramidal and subclasses of interneuron populations in CA1. Our results suggest that Layer 5a of the MEC has a dual function in coordinating neocortical and hippocampal networks.

Results

To find out whether neurons in either L5a or L5b project to the hippocampus we injected retrograde adeno-associated viral vectors (AAVs) expressing green fluorescent protein (GFP) or mCherry into intermediate hippocampus (Figure 1A,B; Figure 1- figure supplement 1A,B). As well as finding retrogradely-labelled cell bodies in layer 3 of MEC, which contains neurons that are well-established as a critical input to stratum lacunosum/moleculare of CA1 (Naber et al., 2001; Kitamura et al., 2014), we also found labelled cell bodies in L5a, which we identified by immunostaining against the ETS variant transcription factor-1 (Etv1) protein. Retrogradely-labelled neurons were not found in L5b.

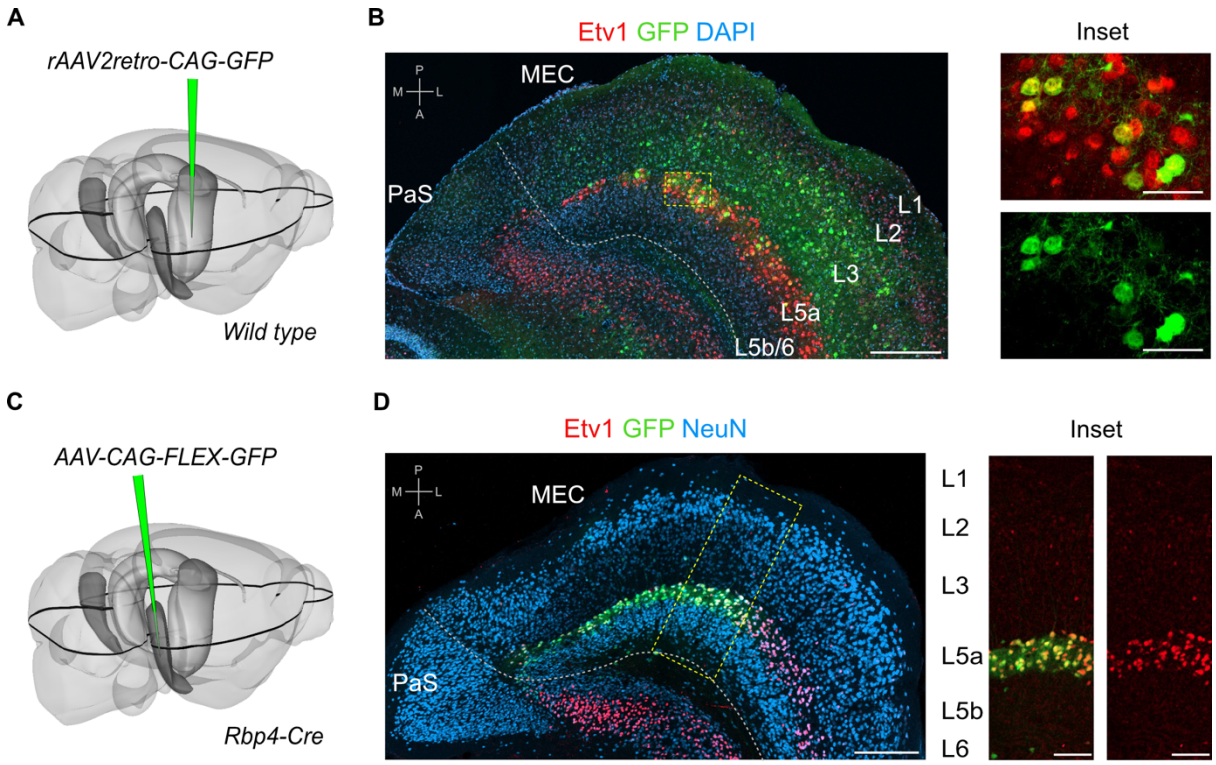

Figure 1. L5a but not layer 5b of the MEC projects to the hippocampus
A, Schematic showing the injection site of a retrograde AAV in the intermediate hippocampus (light grey) of wild type mice. The black outline in the horizontal plane roughly corresponds to the dorso-ventral position of the horizontal section shown in B. Corresponding injection site image is shown in Figure 1- figure supplement 1A.
B, Immunostained brain section in the horizontal plane showing retrogradely-labelled neurons in L3 and L5a of the MEC. Etv1 expression marks L5a (Scale bar: 250 µm). Inset: high-magnification image of boxed region in left panel showing co-expression of GFP and Etv1 (Scale bar: 50 µm). Abbreviations: PaS, parasubiculum; P, posterior; A, anterior; M, medial; L, lateral.
C, Schematic showing the injection site of an AAV in the deep MEC (dark grey) of *Rbp4-Cre* mice for Cre dependent expression of GFP. The black outline in the horizontal plane roughly corresponds to the dorso-ventral position of the slice shown in D.
D, Entorhinal area on an immunostained brain section in the horizontal plane showing the overlapping expression of GFP with Etv1 (Scale bar: 250 µm). Inset: high-magnification of boxed region in middle panel showing GFP and Etv1 expression confined mainly to L5a in MEC (Scale bar: 100 µm).

105 To further investigate this projection, we identified and validated a transgenic mouse line that
106 enables specific genetic access to L5a. In this mouse line, Cre expression is driven by the
107 promoter of the retinol binding protein 4 gene (*Rbp4-Cre*; Gerfen et al., 2013). Following
108 injection of a Cre-dependent AAV expressing GFP or mCherry into the deep MEC of *Rbp4-*
109 *Cre* mice, fluorescent signal was detected mainly in L5a (Figure 1C,D and Figure 1- figure
110 supplement 1C). At the centre of the injection site, where labelling was densest, the majority
111 of neurons in L5a (71.3 ± 2.2 %, n = 3 mice, 180 neurons) were found to be fluorescently
112 labelled (Figure 1D). Labelled neurons were non-GABAergic (99.5 ± 0.3%, n = 3 mice, 1137
113 cells; Figure1- figure supplement 1D), most of which expressed Etv1 (88.6 ± 3.1 %, n = 3

114 mice, 1866 cells; Figure 1D). This is similar to the proportion of Etv1-expression in all L5a
115 neurons (Sürmeli et al., 2015) and also in retrogradely labelled subpopulations of L5a
116 neurons from the hippocampus and from cortical and subcortical target areas (Figure 1-
117 figure supplement 1E,F,G,H). Moreover, axons of L5a neurons labelled in the *Rbp4:Cre* line
118 were found in the telencephalon (Figure1-figure supplement 2). Thus, we established that
119 the *Rbp4-Cre* line provides unbiased genetic access to excitatory projection neurons in L5a.
120
121 To what extent does the projection from L5a to the hippocampus differ from previously-
122 identified projections arising from superficial layers of MEC? In contrast to projections from
123 superficial layers 2 and 3, which respectively target stratum lacunosum (SL) and stratum
124 moleculare (SM) of CA1 (Kitamura et al., 2014), axons from L5a neurons were primarily
125 found in deep stratum pyramidale (SP) and stratum lacunosum (SL), but were sparse in
126 stratum moleculare (SM; Figure 2A,B,C,D and Figure 2- figure supplement 1A). Axons from
127 L5a also differed in their proximo-distal organisation within CA1. Whereas projections from
128 superficial layers of MEC favour proximal CA1 (Tamamaki and Nojyo, 1995), axons from L5a
129 had highest density in distal CA1 (paired one-tailed Wilcoxon signed rank test, $p = 0.0312$, n
130 = 5 mice; Figure 2E,F,G,H and Figure 2- figure supplement 1B,C,D,E,F) and the subiculum
131 (Figure 2I and Figure 2- figure supplement 1G). We observed the same topography when
132 axons and axon terminals of L5a neurons were labelled with membrane-bound GFP and
133 fluorescently-tagged presynaptic proteins (synaptophysin), confirming that the topography is
134 not a result of labelling of passing axons (Figure 2J,K,L,M,N,O). This distinct topography
135 suggests a unique functional role for the projections from L5a of MEC to CA1.
136

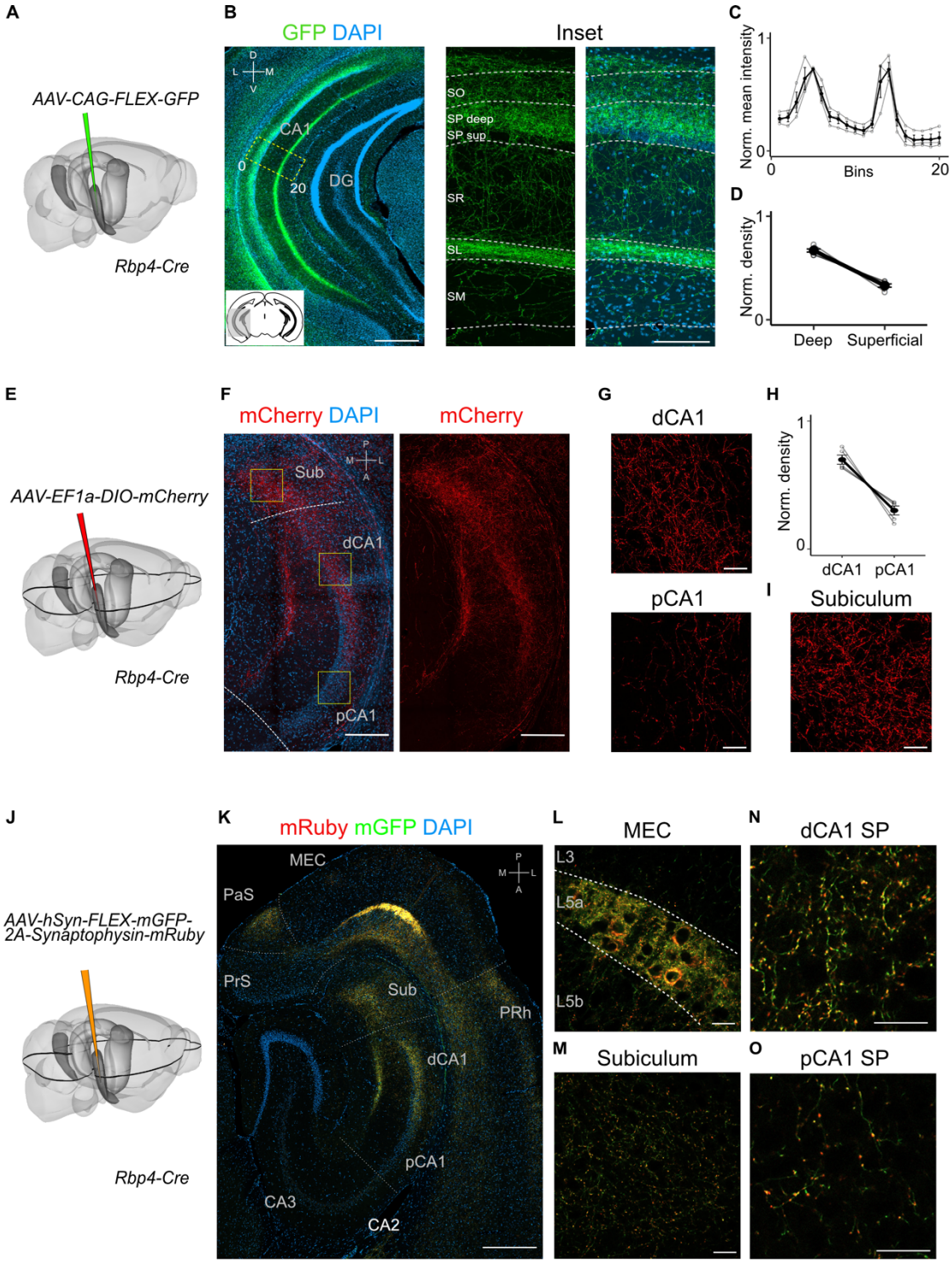
A
AAV-CAG-FLEX-GFP
Rbp4-Cre
B
GFP DAPI
Inset
CA1
DG
SO
SP deep
SP sup
SR
SL
SM
C
Norm. mean intensity
Bins
D
Norm. density
Deep
Superficial
E
AAV-EF1a-DIO-mCherry
Rbp4-Cre
F
mCherry DAPI
mCherry
Sub
dCA1
pCA1
G
dCA1
pCA1
H
Norm. density
dCA1
pCA1
I
Subiculum
J
AAV-hSyn-FLEX-mGFP-2A-Synaptophysin-mRuby
Rbp4-Cre
K
mRuby mGFP DAPI
MEC
PaS
PrS
Sub
PRh
dCA1
pCA1
CA3
CA2
L
MEC
L3
L5a
L5b
N
dCA1 SP
M
Subiculum
O
pCA1 SP

Figure 2. Projections to CA1 of L5a neurons of the MEC have distinct topography
A, Schematic showing the injection strategy of a Cre-dependent virus in the deep MEC of *Rbp4-Cre* mice.
B, Immunostained coronal brain section showing the distribution of axons of MEC L5a cells in CA1 (Scale bar: 500 μm). Inset: high-magnification image of boxed region in left panel (Scale bar: 100 μm). Bottom-left schematic indicates the antero-posterior position of the slice. Corresponding injection site image is shown in Figure 2- figure supplement 1A. Abbreviations: SO, stratum oriens; SP, stratum pyramidale; SR, stratum radiatum; SL, stratum lacunosum; SM, stratum moleculare; D, dorsal; V, ventral; M, medial; L, lateral.
C, Quantification of fluorescence intensity of GFP across the layers of CA1. The area between 0 and 20 in (B) was divided into 20 equally-sized bins, and the mean fluorescence intensity was calculated for each bin. Values shown are normalised mean fluorescence intensity values (n = 6 mice, 2 sections per brain).
D, Normalised mean fluorescence density values in deep versus superficial SP (n = 6 mice). Within SP, axon density in deep SP was significantly higher than density in superficial SP (paired one-tailed Wilcoxon signed rank test, p = 0.0156, n = 6).
E, Schematic showing the injection strategy of a Cre-dependent virus in the deep MEC of *Rbp4-Cre* mice. The black outline in the horizontal plane roughly corresponds to the dorso-ventral position of the horizontal slice shown in (F).
F, Immunostaining of a horizontal brain section showing the distribution of axons of MEC L5a cells in the subiculum (Sub), distal CA1 (dCA1) and proximal CA1 (pCA1; Scale bar: 200 μm). Corresponding injection site image is shown in Figure 2- figure supplement 1B.
G, High-magnification images of the pyramidal cell layer in distal (top) and proximal (bottom) CA1 showing axonal labelling (Scale bar: 20 μm).
H, Normalised mean fluorescence density values in distal versus proximal CA1 (n = 5 mice).
I, High-magnification image of the subiculum showing axonal labelling (Scale bar: 20 μm).
J, Schematic showing the injection strategy of an AAV for Cre-dependent expression of a membrane-bound form of GFP and a synaptophysin-mRuby conjugate in L5a of the MEC in the *Rbp4-Cre* mice. The black outline in the horizontal plane roughly corresponds to the dorso-ventral position of the slice shown in (K).
K, Immunostained brain section in the horizontal plane showing the distribution of axons (green) and synaptic terminals (red) in the hippocampus as well as the parasubiculum (PaS) and perirhinal cortex (PRh). Injection site in the MEC is distinguishable by the strong fluorescent labelling of L5a cell bodies (Scale bar: 400 μm).
L, High-magnification image of the injection site in the MEC showing cell membrane and synaptic labelling specifically in L5a (Scale bar: 20 μm).
M, High-magnification image of the subiculum showing axonal and synaptic labelling (Scale bar: 20 μm).
N,O, High-magnification images of the pyramidal cell layer in distal (N) and proximal (O) CA1 showing axonal and synaptic labelling (Scale bar: 20 μm).

Our findings suggest two intriguing possibilities for the organisation of output neurons in L5a of the MEC. The hippocampus-projecting neurons in L5a may be distinct from the telencephalon-projecting neurons, implying separate processing within the deep MEC layers of signals to the hippocampus and telencephalon. Alternatively, the same neurons in L5a may project to both the telencephalon and the hippocampus, implying that telencephalic outputs from MEC are copied back to the hippocampus. To distinguish between these possibilities we used a combinatorial viral labelling strategy. We restricted reporter gene expression to subpopulations of L5a cells that project to specific targets by injecting a retrograde AAV expressing Cre recombinase in either the retrosplenial cortex (RSC) or

147 nucleus accumbens (NucAcb), and a Cre-dependent fluorescent reporter virus into the MEC
148 (Figure 3A,B and Figure 3- figure supplement 1). With this approach we detected in CA1
149 fluorescently-labelled axons originating from both RSC-projecting and NucAcb-projecting
150 L5a neurons (Figure 3C,D). The axon distribution across layers was similar to when L5a
151 neurons were labelled in bulk using the *Rbp4-Cre* mouse line (Figure 3E,F). These results
152 establish the principle that axon projections from L5a of MEC to the hippocampus are
153 collaterals of projections to telencephalic targets. However, it is unclear from these
154 experiments whether this principle applies to projections from L5a to all of its many
155 telencephalic targets.

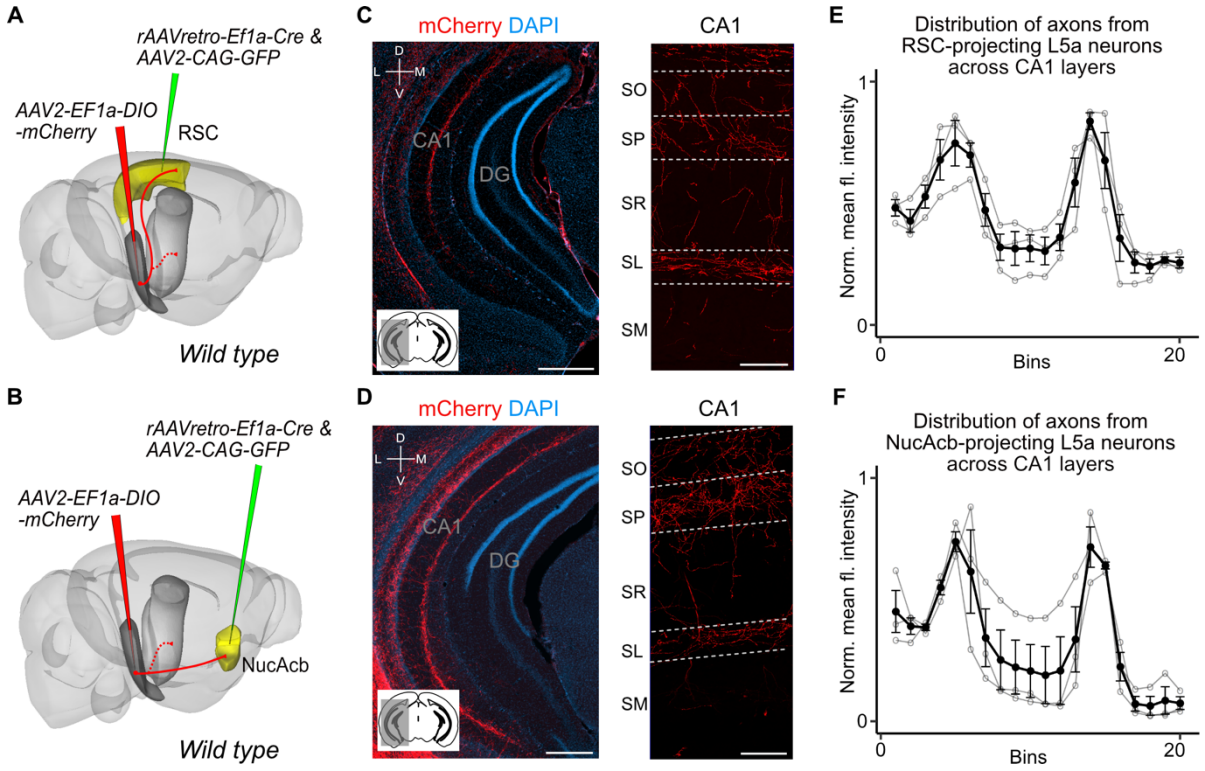

Figure 3. Retrosplenial cortex and nucleus accumbens outputs of the MEC are copied to CA1
A, B, Experimental strategy. In wild-type mice, a retrogradely-transported virus expressing Cre was injected in either the retrosplenial cortex (RSC; A) or nucleus accumbens (NucAcb; B), while a Cre-dependent reporter virus was injected in the deep MEC.
C, D, Hippocampal axon collaterals of RSC-projecting (C) or NucAcb-projecting MEC neurons (D; Scale bar: 250 µm). Insets: high-magnification images from CA1 showing distribution of axons across CA1 layers (Scale bar: 100 µm). Bottom-left schematic indicates the antero-posterior position of the slice. Corresponding injection site images are shown in Figure 3- figure supplement 1A and B.
E, F, Quantification of mean fluorescence intensity across the layers of CA1 when only RSC-projecting (E) or NucAcb-projecting (F) MEC neurons were labelled (n = 3 mice for each group). Axon topography is similar to when L5a neurons are marked globally in the *Rbp4-Cre* mice (Figure 2C).

156 Entorhinal cortex outputs have diverse targets, including the entire cortical mantle as well as
157 parts of basal ganglia and amygdala (Swanson and Köhler, 1986, Sürmeli et al., 2015). To
158 test whether axon collateralisation to the hippocampus is a general feature of all
159 telencephalon-targeting neurons, we used Multiplex Analysis of Projections by Sequencing
160 (MAPseq; Kebschull et al., 2016). We injected the MAPseq barcode RNA virus library into
161 the full dorso-ventral extent of the deep MEC (Figure 4- figure supplement 1A) and
162 quantified barcode RNA expression in tissue collected from dorsal and ventral MEC, dorsal
163 and ventral hippocampus and three major divisions of the brain (isocortex, cerebral nuclei
164 (CNU), olfactory areas and cortical subplate (Olf/Ctxsp), see methods for detailed
165 description, Figure 4A). The majority of barcodes that were detected in any one of the three
166 target divisions (isocortex, CNU or Olf/Ctxsp) were also detected in the hippocampus,
167 suggesting that collateral axons to the hippocampus are a common feature of telencephalon-
168 projecting neurons (Figure 4B). The results were similar regardless of whether neurons were
169 located in dorsal or ventral MEC (Figure 4- figure supplement 1B), suggesting that
170 collateralisation does not depend on the neuron's position in the dorso-ventral axis of the
171 MEC. Using barcode counts as a measure of projection strength (Kebschull et al., 2016) we

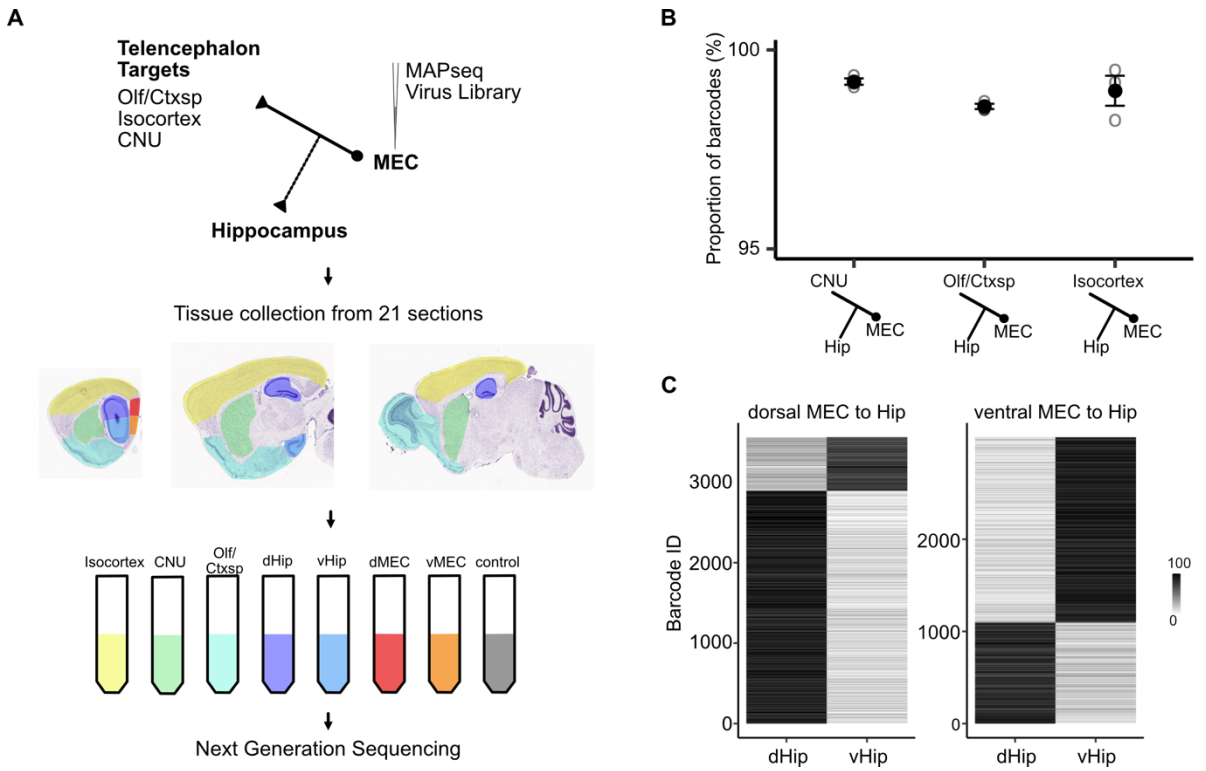

Figure 4. Telencephalic outputs are widely copied onto the hippocampus
A, Experimental strategy. A MAPseq virus library was injected into deep MEC (n = 3). 44 hours later, mice were sacrificed and brains were serially sectioned in the saggital plane at 400 µm thickness. Tissue from 5 major divisions (Isocortex, CNU, Olf/Ctxsp, dHip and vHip), as well as dorsal and ventral MEC were then dissected and collected in tubes. Brainstem tissue was collected as a negative control. Tissue was further processed for RNA extraction and next generation sequencing.
B, Nearly all barcodes detected in CNU, Olf/Ctxsp and Isocortex were also detected in the hippocampus (Isocortex: 98.6% ± 0.06%; CNU: 99.2% ± 0.08%; Olf/Ctxsp: 99.0% ± 0.4%; n = 3 mice, 5358 barcodes).
C, Dorso-ventral topography of projections revealed by relative barcode counts. For each barcode, counts were normalised to show the relative projection strength of each neuron to dorsal and ventral hippocampus (n = 3 mice).

172 further found that dorsal MEC neurons preferentially project to dorsal aspects of the
173 hippocampus and ventral MEC neurons to the ventral aspects, indicating that the back-
174 projections to the hippocampus are topographically organised (Figure 4C). Together these
175 results reveal general organising principles by which all projections from MEC to the
176 telencephalon are copied back to the hippocampus.

177 Which cell types within the hippocampus receive signals from L5a of MEC? While the
178 compartmentalised arrangement of axons from L5a of MEC suggests selective targeting of
179 CA1 layers, axonal topography does not necessarily reflect functional connectivity.
180 Therefore, we targeted viral vectors expressing a channelrhodopsin2-mCherry conjugate
181 to L5a neurons in MEC and tested for connectivity using whole-cell ex-vivo patch clamp
182 recordings from CA1 neurons.

183 We focused initially on responses of pyramidal cells. Brief light pulses evoked depolarising
184 sub-threshold postsynaptic potentials (PSPs) in 64% of SP pyramidal neurons recorded at
185 their resting membrane potential (n = 64 cells, 27 mice, Figure 5A,B,C and Figure 5- figure
186 supplement 1E). The response probability of neurons in distal CA1 was not significantly
187 different than neurons in proximal CA1 (Figure 5D). The majority of PSPs (20 out of 26)
188 maintained their polarity when the membrane potential was adjusted from rest (Vm = -66.7 ±
189 0.6 mV) to -50 mV, indicating that they were glutamatergic. In these neurons EPSPs were
190 maintained when $GABA_A$ receptors were blocked with Gabazine, but were abolished by the
191 AMPA receptor antagonist NBQX, confirming that they are glutamatergic (Figure 5E). The

192 responses had short latencies (3.04 ± 0.26 ms, n = 20 cells, 15 mice) that were relatively

193 invariant from trial to trial (Figure 5F) and were independent of the response's position within

194 a train of stimuli, indicating that they are monosynaptic (Figure 5- figure supplement 1D).

195 Consistent with this, responses were sensitive to bath application of tetrodotoxin (TTX) but

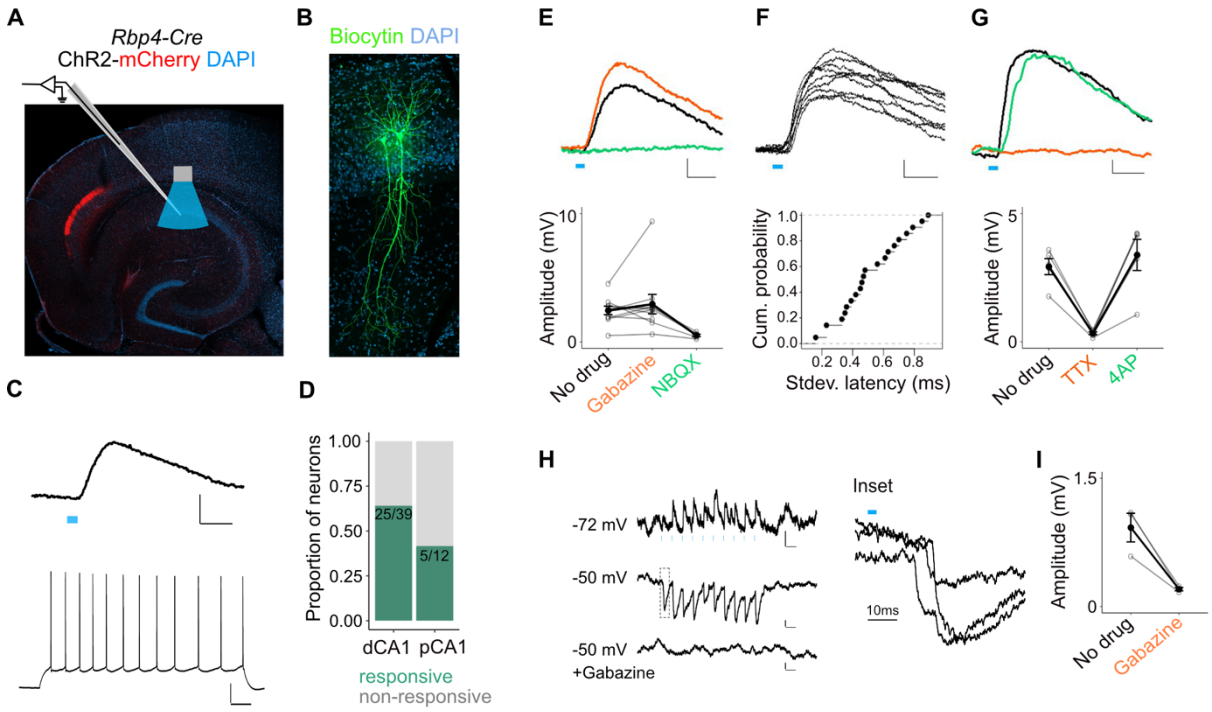

Figure 5. L5a neurons of the MEC provide direct excitatory and indirect inhibitory inputs to pyramidal cells in CA1

A, Experimental design showing viral expression, placement of patch-clamp electrode and light delivery over CA1.

B, Examples of biocytin filled pyramidal neurons recorded in CA1.

C, An example electrical recording of a pyramidal neuron at rest (-67 mV) showing depolarizing responses upon 3 ms light stimulation (top) (blue line, Scale bar: 1 mV, 10 ms). Train of action potentials upon 200pA step-current injection (bottom). (Scale bar: 20 mV, 100 ms)

D, Proportion of responsive pyramidal neurons located in the distal and proximal halves of CA1. The difference in proportions was not significant (X-squared = 1.0932, df = 1, p-value = 0.2958, Chi-squared test, n = 12 cells in proximal and n = 39 cells in distal CA1).

E, Effects of bath application of Gabazine (orange, n = 10 cells, 9 mice) and NBQX (green, n = 5 cells) on PSPs recorded from a pyramidal neuron (Scale bar: 0.5 mV, 10 ms) and a summary plot of PSP amplitude measurements for all tested pyramidal neurons. Note that some neurons were only treated with Gabazine which did not cause a significant change in amplitudes (p = 0.97, 2-tailed Student's t-test, n = 10 cells, 9 mice).

F, An example of ten consecutive PSP responses recorded from a single pyramidal neuron illustrates the short and invariant latency of PSPs (Scale bar: 0.5 mV, 10 ms) and a cumulative probability plot of standard deviation of latencies for neurons with PSP responses that were > 1 mV in amplitude (n = 20 cells).

G, Effects of bath application of TTX (orange) and 4-AP (green) on PSPs recorded from a pyramidal neuron (Scale bar: 0.5 mV, 10 ms) and a summary plot of changes in PSP amplitudes for all tested pyramidal neurons. TTX application abolished responses (n = 5 cells, 5 mice, p = 0.01, 2-tailed Student's t-test).

H. An example inhibitory PSP response recorded from a pyramidal neuron upon 10 Hz light stimulation (blue bars). Response polarity reversed when the neuron's membrane potential was adjusted to -50 mV and was abolished after application of Gabazine (Scale bars: 0.2 mV, 100 ms). Inset shows the long latency (> 10 ms) of PSP onset indicating polysynaptic connectivity.

I. Effects of bath application of Gabazine on the response amplitude of long latency PSPs (n = 3 cells).

196 recoverable after application of 4-Aminopyridine (4-AP; Figure 5G; Petreanu et al., 2007).
197 Together, these data demonstrate that projections from L5a of the MEC provide
198 glutamatergic excitatory inputs directly to pyramidal neurons in proximal and distal CA1.
199
200 A smaller population of pyramidal neurons showed PSPs with characteristics of indirect
201 inhibitory connections (6 out of 26). These responses either reversed polarity when the cell
202 was held above the chloride reversal potential (Figure 5H) or had an early depolarising and a
203 late hyperpolarising component (Figure 5- figure supplement 1B). Application of Gabazine
204 either completely blocked the PSPs (Figure 5I) or revealed a larger excitatory component
205 that was sensitive to application of NBQX (Figure 5- figure supplement 1B). Thus, inputs
206 from L5a of the MEC also recruit local interneurons that provide inhibitory input to SP
207 pyramidal neurons.
208
209 To identify which interneurons in CA1 were targets of L5a projections, we tested responses
210 of interneurons in all layers. In SP we distinguished interneurons from principal cells either
211 by classifying them based on biophysical properties (fast-spiking: SP_{FS} and non-fast spiking:
212 SP_{NFS} ; Figure 5- Figure supplement 1a and see methods), or by recording from
213 fluorescently-labelled GABAergic or parvalbumin-expressing (PV+) inhibitory neurons in
214 double transgenic mice (Figure 6A,B and Figure 5- figure supplement 1C). Stimulation of
215 L5a axons elicited both sub-threshold and supra-threshold responses primarily in SP, SR
216 and SL interneurons (Figure 6C,D and Figure 5- figure supplement 1E). Depolarising PSPs
217 were observed in 64% of the SP_{FS} including PV+ interneurons, 46% of the SP_{NFS}, 64% of SR
218 and lower proportions of recorded neurons in SL (31%), SM (23%) and SO (16%). Except for
219 interneurons in SO, PSPs in all layers showed characteristics of monosynaptic connectivity
220 (Figure 6G,H,I,J and Figure 5- figure supplement 1G,H) and AMPA receptor-mediated
221
222

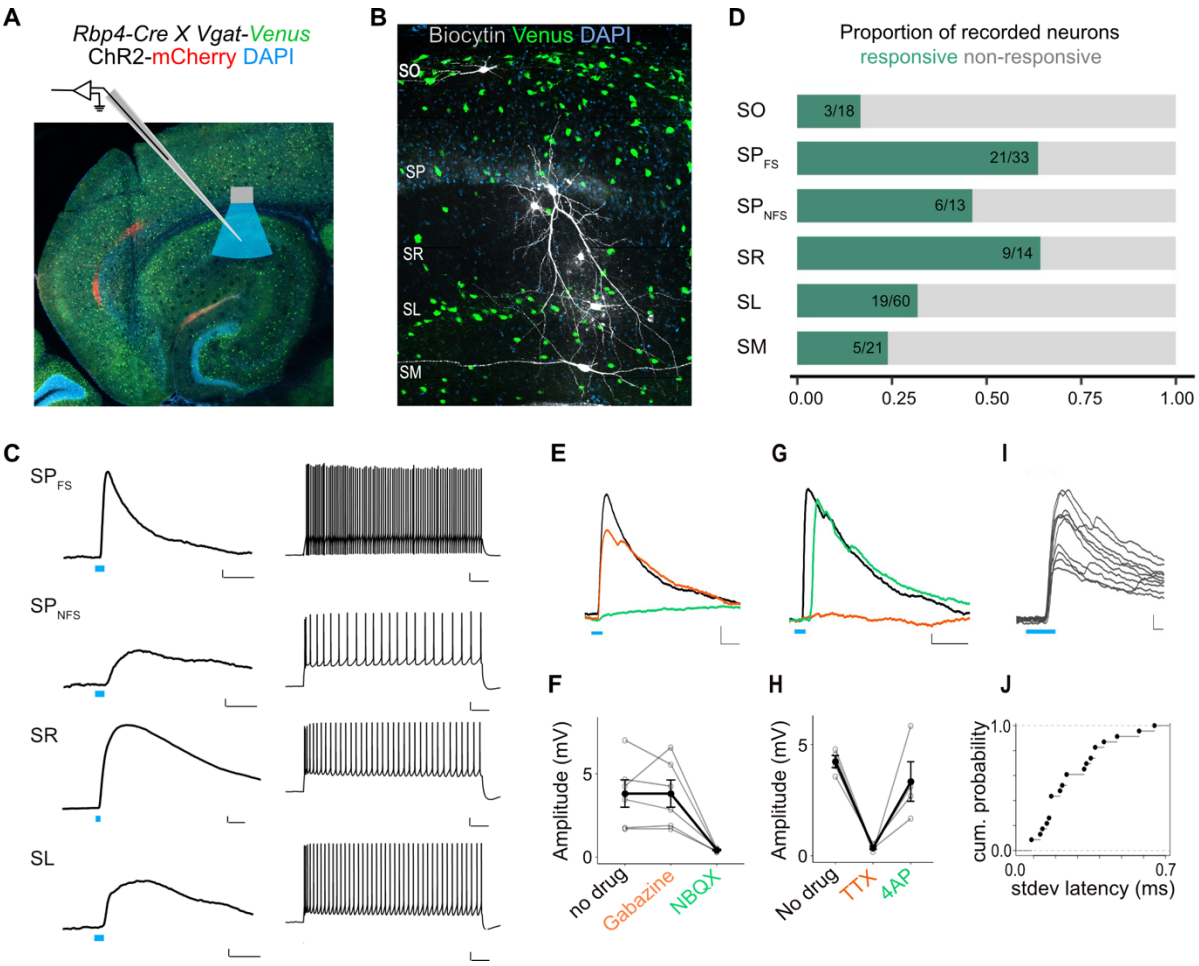

Figure 6. L5a neurons of the MEC provide direct excitatory inputs to interneurons in CA1.
A, Experimental design showing viral expression, patch pipette and light stimulation. Interneurons are marked by the expression of venus fluorescent protein driven by the vesicular GABA transporter (*Vgat*) gene's promoter.
B, Biocytin filled neurons in the *Rbp4-Cre X Vgat-Venus* double transgenic mouse line. Fluorescent labelling facilitated patch-clamp recordings made from GABAergic interneurons and distinguishing SR, SL and SM layers.
C, Representative examples of depolarising responses recorded at resting membrane potential following 3 ms blue light stimulation (blue line) of L5a axons in CA1 (left) (Scale bar: 1 mV, 10 ms). Neurons in SO and SM were typically not responsive (< 30%). Responses from SR neurons were on average larger than the responses from neurons in other layers (Scale bar: 1 mV, 10 ms). Neurons' spiking response to injecting 200 pA current (right) (Scale bar: 10 mV, 100 ms).
D, Proportion of responsive interneurons in all layers of CA1 recorded at resting membrane potential. Green highlighted segment corresponds to the proportion of cells with depolarising membrane potentials; grey highlighted segment corresponds to neurons with no change in their membrane potential.
SO: n = 18 cells, 10 mice;
SP_{FSint} : n = 33 cells, 8 *Rbp4-Cre X Pvalb-Flp mice*, 5 *Rbp4-Cre X Vgat-Venus mice*, 8 *Rbp4-Cre* mice;
SP_{NSFint}: n = 13 cells, 11 *Rbp4-Cre* mice, 1 *Rbp4-Cre X Vgat-Venus* mouse;
SR: n = 14 cells, 6 mice; SL: n = 60 cells, 15 mice; SM: n = 21 cells, 10 mice
E,F, Effects of bath application of Gabazine (orange) and NBQX (green) on PSPs recorded from a fast-spiking pyramidal layer interneuron (left) (Scale bar: 1 mV, 5 ms)**.** Summary quantification of PSP amplitudes for multiple cells (right). The PSP amplitudes were largely unaffected by application of Gabazine (SP_{int} : n = 6 cells, p = 0.99 2-tailed Student's t test) but were largely blocked by NBQX (SP_{int} : n = 5 cells, p = 0.03, 2-tailed Student's t test) indicating AMPA receptor mediated glutamatergic synaptic transmission.
G,H. Effects of bath application of TTX (orange) and 4-AP (green) on the response amplitude PSPs recorded from pyramidal layer interneurons. Example traces from a fast-spiking pyramidal layer interneuron (Scale bar: 1 mV, 5 ms). Summary plots of response amplitude measurements from multiple recordings (SP_{int}: n = 4 cells).
I, J, An example of ten consecutive PSP responses recorded from a single fast-spiking interneuron in SP illustrates the short and invariant latency of PSPs. Cumulative probability plots of standard deviation of latencies for neurons with PSP responses that were > 1 mV in amplitude (mean latency SP: 2.08 ± 0.08 ms, n = 21 cells).

223 glutamatergic synaptic transmission (Figure 6E,F and Figure 5- figure supplement 1F).

Therefore, projections from L5a of MEC recruit CA1 interneurons through monosynaptic inputs driven by excitatory glutamatergic synapses.

Discussion

Together our results suggest a substantial revision to the idea that the entorhinal deep layers unidirectionally convey hippocampal output messages to the neocortex. Using two lines of evidence, combinatorial viral labelling and MAPseq, we show that L5a axons bifurcate to target both the telencephalon and the hippocampus. Our results imply that nearly all telencephalic output is copied onto the hippocampus regardless of its destination in the telencephalon. There is a topographical register between the dorso-ventral origin of the entorhinal cells and their target zone within the hippocampus. This is similar to the dorso-ventral topography of perforant-path projections of the superficial EC targeting the dentate gyrus, supporting the view that dorso-ventral compartments of the hippocampus operate independently (Ruth et al., 1982; Dolorfo and Amaral 1998). Interestingly in the transverse axis, the density of projections has a gradient descending towards proximal CA1 (towards CA2). This is in contrast to previous reports where labelling of MEC projections using traditional tracers revealed dense projections in proximal but not in distal CA1 (Tamamaki and Nojyo, 1995; Naber et al., 2001). Instead, distal CA1 is thought to be primarily targeted by the lateral EC. The distinct organization of projections originating in L5a of the MEC that we reveal here suggests that they serve functions distinct from the projections targeting CA1 from superficial layers instead of merely supplementing them (Witter et al., 2017). This also opens a possibility for the lateral and medial entorhinal cortex input streams to converge in CA1.

Although cells in deep entorhinal layers have been previously observed when retrograde dyes were placed in the CA1-subiculum border (Köhler, 1985; Witter and Amaral, 1991) the tools we introduced in this study made it possible to investigate the layer origin of these

projections and their targets within CA1 with cell type specific anterograde labeling. Our observation that L5b does not participate in this pathway reinforces the distinct input-output organisation of the deep MEC. While L5b is a point of integration for local and neocortical input with hippocampal output and distributes its signals locally within MEC, L5a appears to be suited to coordinate the wider hippocampal-neocortical loop by providing a copy of entorhinal output back to CA1.

Finally, our findings raise new questions about the functional roles of outputs from the entorhinal cortex, and about the nature of interactions between the entorhinal cortex and the hippocampus. Telencephalic projections of L5a cells have been shown to be necessary for long-term memory formation and retrieval (Kitamura et al., 2017), likely by distributing compressed hippocampal outputs to the neocortex (McClelland et al., 1995). Returning a copy of these outputs back to CA1 might create a self-reinforcing or a self-correcting loop. They might also provide a gating signal to modulate the impact in CA1 of inputs from CA3 (Dudman et al., 2007) and/or neocortical return inputs via L3 of EC. It is also conceivable that they influence mechanisms of learning and memory by affecting rhythmic network activity through the inputs on the pyramidal cells and interneuron populations that we described here (Colgin 2016; Ognjanovski et al. 2017; Xia et al. 2017).

Methods

Mice

All animal experiments were approved by the University of Edinburgh animal welfare committee and were performed under a UK Home Office project license. The *Rbp4-Cre* mouse line was generated by GenSat and obtained from MMRRC (*Tg(Rbp4-cre)KL100Gsat/Mmucd*). The *Vgat-Venus* mouse line was generated by Dr. Atsushi Miyawaki at RIKEN, Wako, Japan(Wang et al., 2009). The *Pvalb-Flp* mouse line was obtained from Jackson Laboratories *(B6.Cg-Pvalb-tm4.1(FlPo)Hze/J; Jax 022730)*. Wild-type mice were obtained from Charles River Laboratories C57Bl6J stock. Double transgenics were generated by crossing the *Rbp4-Cre* line to the *Vgat-Venus* or the *Pvalb-Flp* lines. *Rbp4-Cre* and *Pvalb-Flp* lines were maintained as heterozygous and all mice were on C57Bl6 background.

Viral constructs and injection strategy

8 to 14 week-old male and female mice were used in all experiments. For targeting deep MEC a craniotomy was made 3.4 to 3.65 mm lateral to the bregma (X) between the transverse sinus and lambdoid suture (Y = 4.5 to 5 mm caudal to bregma). The injection pipette was at a 9 degree angle towards the caudal end of the brain. 100 nl of virus was slowly released at four Z-depths 3.0, 2.8, 2.6 and 2.4 mm from the surface of the brain. 3 mins after delivering the virus the injection needle was retracted to the next injection depth until the most dorsal location where 10 mins past before the needle was fully retracted. For anterograde tracing of L5a axons and terminals *AAV-EF1a-DIO-mCherry* (serotypes 2 and 5, titer 5.3 x 10^{12}, lot #AV4375H, K., Deisseroth, UNC Vector Core), *AAV-CAG-FLEX-GFP* (titer 3.7 x 10^{12}, lot #AV4530B, E. Boyden, UNC Vector Core) and AAV-hSyn-FLEx-mGFP-2A-Synaptophysin-mRuby (Addgene:71760) were used.

301 For injections in CA1 a craniotomy was made 3.5 mm lateral and 3.30 mm caudal to the
302 bregma in C57BL6J mice. 100nl virus was delivered at 3.0, 2.8, 2.6, 2.4 and 2.2 mm from
303 the surface. For retrograde labelling of hippocampus-projecting EC neurons, 100nl of a
304 *rAAV2retro-CAG-GFP* (titre 3.5 x 10^{12}, lot #AV7493D, E. Boyden, UNC Vector Core) or
305 *rAAV2retro-hSyn-mCherry* (E. Boyden, UNC Vector Core) was injected at each depth.

306 To assess whether telencephalic projection neurons in L5a of MEC co-express Etv1 (Figure
307 1- figure supplement 1D), fluorophore coupled choleratoxin beta subunit (CTB-Alexa 488
308 and CTB-Alexa 555) was injected at various sites in wild-type mice as previously described
309 (Sürmeli et al., 2015) and coexpression of Etv1 and Alexa dyes were examined in confocal
310 images.

311 To achieve Cre expression in target specific subpopulation of L5a neurons in the MEC
312 (Figure 3) a *rAAVretro-EF1a-Cre-WPRE* (viral construct was a gift from Karl Deisseroth, titre
313 2.4 x 10^{12}) was made using an AAV-retro helper plasmid (Addgene plasmid ID 81070) as
314 described previously(McClure et al., 2011). A cocktail of *rAAVretro-EF1a-Cre-WPRE* and
315 *AAV-CAG-GFP* (titer 4.3 x 10^{12}, lot #AV6951B, Boyden, UNC Vector Core) viruses were
316 injected either in NucAcb (X: +1.0 mm; Y: +1.2 mm; Z: -3.8, -4.0 mm) or RSC (X: +0.4 mm;
317 Y: -2.8, -3.2 mm; Z: -0.9 mm) in wild-type mice. A Cre inducible reporter virus was also
318 injected in the MEC as described above. GFP expression driven by the *CAG* promoter at the
319 target site was used for verification of injection location.

320 To achieve expression of channelrhodopsin-2 in L5a axons, we injected *AAV2-EF1a-DIO-*
321 *hChR2(H134R)-mCherry-WPRE-pA* (titer 5.1 x 10^{12}, lot #AV4319J, Deisseroth) in the MEC
322 of the *Rbp4-Cre* or the *Rbp4-Cre X Vgat-Venus* or the *Rbp4-Cre X Pvalb-FLP* double
323 transgenic mice. Additionally, in order to fluorescently label parvalbumin expressing
324 interneurons in CA1 a Flp recombinase-dependent AAV vector was constructed in house
325 and injected in the hippocampus (X: +3.0 mm; Y: -3.5 mm; Z: -2.0, -3.0 mm, 200 nl virus was
326 injected at each Z-depth). To produce the virus, the viral construct pAM-FLEX-GFP(Murray

327 et al., 2011) (a gift from Peer Wulff) was used as the viral backbone. The eGFP, loxP and
328 lox2272 sites were removed and replaced with a synthesised cassette (GenScript)
329 containing a multiple cloning site flanked by two sets of heterotypic (FRT and F3),
330 antiparallel FRT sites to produce pAM FLPX. For pAM FLPX eGFP and pAM FLPX mCherry,
331 the fluorescent proteins were amplified from pAM FLEX eGFP and pmCherry-C1 (Clontech)
332 respectively, with EcoRI and SacI overhangs and cloned into pAM FLPX. All AAV preps
333 were generated in house as previously described(McClure et al., 2011) and were titered by
334 qPCR following expression in HEK cells (> 10^{12} genome copies (GC)/ml).

335 Tissue processing and immunohistochemistry

336 3 to 4 weeks after the virus injection surgery, mice were transcardially perfused with 4%
337 paraformaldehyde as previously described(Sürmeli et al., 2015). Brains were sectioned at 60
338 µm using a cryostat (Leica CM3050 S) either coronally or horizontally and sections were
339 stored in PBS at 4°C. All subsequent incubation and washing steps were carried out at 4°C.
340 Prior to antibody staining, sections were blocked with either 5% normal goat serum (NGS;
341 Abcam: ab13970) or 2% bovine serum albumin (BSA; Sigma: A9418) in 0.3% PBST (PBS
342 with 0.3% Triton-X100) for 2hrs. Sections were then transferred to primary antibody solutions
343 made with either 5% NGS or 2% BSA in 0.3% PBST and incubated overnight. After 3
344 washes, each 20 min, in 0.3% PBST, sections were transferred to secondary antibody
345 solutions made with 0.3% PBST and, if required, NeuroTrace 640/660 (1:800; Life
346 Technologies: N21483) and incubated overnight. After 3 washes, sections were incubated in
347 DAPI (1:2,000; Sigma Aldrich: D9542) solution made in PBS for 20 min at room temperature,
348 where required, and then mounted on microscope slides using Mowiol® 4-88 (Aldrich:
349 81381). Slides were covered with glass coverslips and left to dry overnight at 4°C in the dark.
350 The following primary antibodies were used: rat anti-mCherry (1:2,000; ThermoFisher:
351 M11217), chicken anti-GFP (1:10,000; Abcam: ab13970), rabbit anti-Etv1(Arber et al., 2000)
352 (1:1,000), chicken anti-NeuN (1:1,000; Sigma Aldrich: ABN91). The following secondary

353 antibodies from Thermo Fisher Scientific were used at a concentration of 1:800: goat anti-
354 rabbit A488 (A11034), goat anti-chicken A488 (A11039), goat anti-rat A555 (A21434) and
355 goat anti-rabbit (A21244).

356 Cell counting

357 Every 4th brain section was imaged as a Z-stack (1 µm step size) using either the Zeiss
358 LSM 800 (Zen, v2.6.76) or Leica SP8 confocal microscope (Leica Application Suite X,
359 v3.5.6.21594) at 20x magnification. Regions of interest were drawn around L5a and cell
360 counting was carried out either manually using Fiji software or using cell-counting tools in
361 Vision4D (Arivis, v3.2.0).
362
363 The boundaries for L5a were determined using either a DAPI or Neurotrace counterstain.
364 The border between medial and lateral divisions of EC was determined in each section using
365 layer 2 as a guide – in lateral EC, layer 2 is separated into two distinct layers, while this
366 separation is not seen in medial EC(Cappaert et al., 2015).

367 Quantification of the distribution of fluorescent signal

368 *Quantification of fluorescence across the radial axis of the CA1*

369 The distribution of axons of L5a neurons in the radial axis of the hippocampal CA1 was
370 quantified in slide-scanner images (Figure 2) or confocal images (Figure 3) using Fiji
371 software. Coronal brain sections between 3.28 to 3.58 mm posterior to Bregma, which
372 contain distal CA1, were selected for analysis. 2 sections from each brain in which the
373 fluorescent labeling was representative of all the sections were used. DAPI was used as a
374 counterstain. In each section, a 400 µm-wide rectangular ROI was drawn across the radial
375 axes, covering all layers of a randomly selected region in intermediate CA1 (Figure 2B). This
376 ROI was then divided into 20 equal bins and the mean fluorescence intensity was calculated

377 for each bin. The mean intensity values were then normalised in each brain by scaling the
378 values such that the highest value is 1.

379 *Quantification of fluorescence in the transverse axis of the CA1*

380 A Zeiss Axioscan slidescanner was used to image every second brain section at 10x
381 magnification. The projection strengths of MEC L5a neurons to proximal and distal halves of
382 CA1 were quantified in horizontal sections located at depths between 2.56 mm to 4.12 mm
383 from the surface of the brain, with injection sites located across medial, mid and lateral MEC
384 (15-18 brain sections per mouse, n = 5 mice). GFP and mCherry fluorescence signals were
385 amplified with immunostaining as described previously. The borders of CA1 were drawn on
386 brain section images using a customisable digital microscopy analysis platform (Visiopharm),
387 and the proximo-distal border was defined as the border equidistant from the proximal and
388 distal ends of CA1. The mean fluorescence density, defined as the total number of pixels
389 above a set threshold in an area divided by the total number of pixels in the area, was
390 measured in proximal and distal CA1. The threshold was determined manually by ensuring
391 that only pixels representing axons were detected as signal. A median unsharp background
392 correction was used to remove background noise from axons outside of the focus plane of
393 the image. The mean fluorescence density values were then normalised within each brain by
394 scaling the values such that the total fluorescence density value (proximal + distal) in each
395 brain is equal to 1.

396 The spread of viral expression in MEC was assessed from the fluorescent signal in all
397 sections for each brain. Brains in which labelled neurons were found outside L5 were
398 excluded; this was a result of occasional and sparse labelling in L2 or L3 or the
399 parasubiculum in the *Rbp4-Cre* line.

400 MAPseq

401 5 C57Bl6J adult male and female mice were injected in the deep MEC with the MAPseq
402 Sindbis viral barcode library (3 x 10^{10} GC/ml) provided by the MAPseq facility (Cold Spring
403 Harbor Laboratories). To cover the whole mediolateral and dorsoventral extent of the MEC
404 virus was injected in two locations: 3.4 mm and 3.6 mm lateral to bregma. 100 nl virus was
405 delivered to 3.0, 2.8, 2.6, 2.4 mm below the surface of the brain. After 44 hrs, mice were
406 sacrificed, brains were extracted and immediately immersed in oxygenated cold ACSF
407 prepared in ultrapure water. All surgical tools and surfaces were treated with RNaseZAP
408 (Invitrogen) prior to the start of the experiment and in-between samples. 400 µm fresh
409 sagittal brain sections were cut using a vibratome(Pastoll et al., 2012). Immediately after
410 this, GFP expression in the deep EC was verified under a fluorescent microscope and tissue
411 was dissected in cold oxygenated ACSF using microdissection blades on sylgard covered
412 petri dishes which were kept on ice. Each slice was dissected on a previously unused
413 surface of the plate with fresh ACSF and a dedicated microblade was used for the dissection
414 of each brain division to prevent contamination. Tissue pieces were collected into bead
415 containing (Qiagen 69989) collection tubes (Qiagen 19560) on dry ice. After tissue
416 collection, 400 µl Trizol (Thermo Fisher Scientific #15596026) was added to each collection
417 tube. The procedure was repeated for all 5 brains. 3 brains with the largest coverage of MEC
418 deep layers were selected to proceed to the next steps. Tissue was stored at -80 degrees
419 before it was shipped on dry ice to CSHL MAPseq core facility for further processing. RNA
420 extraction, production of double stranded cDNA, library preparation and Illumina sequencing
421 and preprocessing of sequencing data was performed by the MAPseq core facility as
422 described in(Kebschull et al., 2016).

423 For the tissue dissections, identification of brain areas was done by using Allen Brain
424 Reference Atlas (https://mouse.brain-map.org/). The isocortex division included the
425 somatosensory, motor, visual, posterior parietal, anterior cingulate and retrosplenial areas
426 combined. The cerebral nuclei (CNU) division was restricted to striatum. The
427 olfactory/cortical subplate division (Olf/Ctxsp) was a combination of olfactory areas and

428 cortical subplate including amygdalar nuclei. The remaining two divisions were dorsal (dHip)
429 and ventral hippocampus (vHip) including subiculum. Some brain areas were excluded from
430 the study because of the difficulty in dissecting or identifying brain areas in the sagittal plane.
431 All sections > 3.7 mm lateral to bregma are not annotated in Allen Brain Reference Atlas and
432 were excluded. Therefore, neocortical areas in the most lateral sections such as perirhinal
433 cortex, ectorhinal cortex, temporal association areas were not included in the study. The
434 claustrum and adjacent neocortical areas (visceral, agranular insular, gustatory) were
435 excluded as it was not possible to separate these areas precisely to prevent contamination
436 between the assigned divisions. Since borders between the brain divisions CNU and
437 OLF/Ctxsp were not always clear, dissections avoided these areas hence the brain areas in
438 these divisions are partially included. White matter between the hippocampus and the
439 neocortex carrying axon tracts were also excluded. Brainstem and cervical spinal cord tissue
440 were used as control. When L5a neurons in the MEC were labelled using strategies
441 explained in Figure 2, no axonal projections to these areas were observed (unpublished
442 experiments). Consistent with this, a low number of barcodes were identified in the negative
443 control samples (on average 1.0% of barcodes had counts in control areas, n = 3).

444 A limitation of the barcode-based single-cell tracing method comes from the possibility of
445 multiple neurons being represented by the same barcode. This is prevented by adjusting the
446 barcode diversity and the size of the target population as explained in detail in(Kebschull et
447 al., 2016). In order to assess the expected fraction of uniquely labelled neurons in our study
448 we counted the total number of neurons in L5a of the MEC. A total of 2314 ± 131, (n = 2
449 mice) NeuN-labelled neurons were counted. Using the formula $F = (1-(1/N))^{k-1}$ where N is
450 the barcode diversity (2×10^6)(Kebschull et al., 2016) and k is the number of infected
451 neurons the predicted ratio of uniquely labelled neurons is 99.9%. Multiple representation of
452 neurons due to a neuron being infected by several different barcode RNA-expressing viral
453 particles was not corrected for since the projection patterns are not affected by
454 overrepresentation of neurons(Kebschull et al., 2016).

455 *MAPseq data analysis*

456 Barcode counts were first normalised in each area by the relative number of spike-in RNAs
457 for each sample. Orphan barcodes, barcodes which did not have counts in the injection site,
458 (dMEC or vMEC) were removed. We then calculated the 95th percentile of the barcode
459 counts in our negative controls and based on this set all barcode counts of 1 to 0. A small
460 number of barcodes had a higher count in any target area compared to the injection site
461 which might be a result of incomplete dissection of the injection site or viral expression in
462 areas that the virus spilled into as we retracted the pipette. These barcodes were removed.
463 Since our goal was to find whether neurons projecting to the telencephalon also project to
464 the hippocampus we removed the barcodes that had no counts in any of the telencephalic
465 target areas. For the same reason, barcodes that were detected only in the dHip or vHip
466 hippocampus were also removed. Finally, we excluded all barcodes with counts of less than
467 400 in the injection site to minimise the possibility of incomplete transport of RNA barcodes
468 to axons in target areas due to weak expression at the cell bodies or low counts due to PCR
469 or polymerase errors. Barcodes with low counts in all target areas (< 10) were also excluded
470 to account for potential false positives.

471

472 To quantify the proportion of barcodes that were present in both a target division (Figure 3H;
473 Isocortex, CNU or Olf/Ctxsp) and the hippocampus, the following formula was used: (total
474 number of barcodes with counts detected in both hippocampus and target division / total
475 number of barcodes with counts detected in target division). To compare the difference
476 between barcodes with the injection site in dMEC vs vMEC, the barcodes were divided into
477 two groups – “dorsal MEC”, where counts in dMEC were higher than in vMEC, and vice
478 versa for “ventral MEC”. A paired two-tailed Wilcoxon signed rank test was used to check if
479 there was a significant difference between the proportion of collateralising neurons in dMEC
480 and vMEC.

481

482 To visualise the distribution of barcode counts in dHip and vHip from “dorsal MEC” or
483 “ventral MEC” groups, we generated heat maps showing normalised projection strengths
484 between dHip and vHip for all barcodes. The normalised projection strengths were
485 calculated by the formula: projection $strength_{dHip}$ = ($counts_{dHip}$) / ($counts_{dHip+vHip}$) * 100, and
486 likewise for vHip. Barcodes were sorted by maximum projection site.
487

488 Ex-vivo electrophysiology

489 *Slice preparation*

490 Slice preparation and subsequent data acquisition was done as previously
491 described(Sürmeli et al., 2015). 3 to 4 weeks after the injection of the viral vectors ex-vivo
492 brain slices were prepared. Following decapitation, brains were immersed for 2 mins in 4°C
493 artificial cerebrospinal fluid (ACSF) of the following composition (mM): 86 NaCl, 1.2
494 NaH_2PO_4, 2.5 KCl, 25 $NaHCO_3$, 25 Glucose, 75 Sucrose, 0.5 $CaCl_2$, 7 $MgCl_2$, bubbled with
495 95% O_2 / 5% CO_2. They were then sectioned horizontally (400 µm) using a vibratome (Leica
496 VT1200) ACSF. Tissue was collected and maintained in extracellular solution of the
497 following composition (mM): 124 NaCl, 1.2 NaH_2PO_4, 2.5 KCl, 25 $NaHCO_3$, 20 Glucose, 2
498 $CaCl_2$ and 1 $MgCl_2$, continuously supplied with 95% O_2 / 5% CO_2. Slices were allowed to rest
499 for 15 mins at 35°C followed by a minimum of 30 mins recovery time at room temperature
500 before the start of the experiment.

501 *Electrophysiological recordings*

502 Whole-cell patch-clamp recordings were made in pyramidal neurons and interneurons in all
503 layers of hippocampal CA1. Typically, 2 to 3 slices from the intermediate hippocampus were
504 used where morphologies of the pyramidal cells and interneurons were confirmed to be
505 intact with post hoc staining and imaging of biocytin filled neurons. Data was collected using
506 AxoGraph (v1.7.6) software.

507 Pipettes with 4 to 6 MΩ resistance were pulled from borosilicate glass (Sutter Instruments)
508 and filled with an intracellular solution of following composition (mM): 130 K Gluconate, 10
509 KCl, 10 HEPES, 2 $MgCl_2$, 0.1 EGTA, 2 Na_2ATP, 0.3 Na_2GTP, 10 NaPhosphocreatine, 5.4
510 Biocytin. The intracellular solution was adjusted to a pH of 7.2 to 7.4 with KOH and
511 osmolarity 290-300 mOsm. All recordings were made in current clamp mode with pipette
512 capacitance neutralisation and bridge balance applied. Subthreshold membrane properties
513 were measured from the changes in membrane potential upon depolarising and
514 hyperpolarising current injections (typically -40 pA to +40 pA, in 20 pA). Rheobase was
515 established from responses to a depolarizing current ramp (50 pA/sec, maximum current
516 400 pA).

517 For optogenetic stimulation of ChR2, an LED of wavelength 470 nm (ThorLabs) was
518 attached to the epifluorescence port of the microscope. Where necessary, the irradiance of
519 the LED (max 9 mW) was controlled by voltage commands. Pharmacological tests were
520 done by bath application of the following reagents with the indicated final concentrations in
521 standard extracellular solution: Gabazine (10 μM, Hello Bio, Cat. No. HB0901), NBQX (10
522 μM, Tocris, Cat. No. 0373), D-AP5 (50 μM, Tocris, Cat. No. 0106), 4-AP (200 μM, Tocris,
523 Cat. No. 0940), TTX (1 μM, Hello Bio). To allow for morphological reconstructions cells were
524 filled with Biocytin (5.4 mM in intracellular solution, Sigma, Cat. No. B4261) during
525 electrophysiological recordings.

526 *Analysis of electrophysiological recordings*

527 Electrophysiological properties were analysed using built-in and custom routines in
528 IGORpro8 (WaveMetrics) and Matlab (MathWorks). All basic properties were established
529 from the I-V protocol described above. Input resistance was determined from the largest
530 depolarising current step injected. Sag ratio was calculated as $V_{steady\ state}$/ V_{min} from the largest
531 hyperpolarising current step. Rheobase and action potential (AP) threshold were determined
532 from the first AP during injection of steadily increasing current in a ramp. From the same

533 protocol, after-hyperpolarisation (AHP) was calculated as the difference between AP
534 threshold and the most negative peak of the hyperpolarisation following the first spike. Half-
535 width was measured as the width of the AP at half its maximum spike amplitude. Firing
536 frequency was measured from a 1 s current injection of 200 pA. Maximum firing frequency
537 was measured between the first two APs, and base frequency between the last two APs in a
538 train.

539 For optogenetic stimulations, responsiveness was confirmed for each cell by a significant
540 difference between the detected peak of change in membrane potential after light stimulation
541 and the average baseline using a 2-tailed, type 1 student's t-test. The PSP amplitude and
542 latency were measured using the Neuromatic toolbox in IGORPro8.

543 Cell types were determined based on biophysical properties extracted from
544 electrophysiology data. Pyramidal cells were identified from a max firing frequency of < 50
545 Hz, AHP < 10 mV, AP half-width ≥ 0.7 ms and sag ≤ 0.9, with descending hierarchical order.
546 Fast spiking interneurons were categorised from a max firing frequency ≥ 100 Hz, AHP ≥ 12
547 mV, AP half-width < 0.5 ms and sag > 0.9. Non-fast spiking interneurons were classified
548 from a max firing frequency 50-100 Hz, AHP ≥ 12 mV, AP half-width 0.5 to 0.9 ms, sag ratio
549 > 0.9. and max firing frequency 50-100 Hz.

550 Neurons with a resting membrane potential less negative than -50 mV or a bridge balance
551 higher than 40 MΩ were excluded from the analysis, as were neurons that did not fit within a
552 class from above criteria.

553 *Immunostaining of electrophysiology slices*

554 For identification of cells following recordings, tissue was fixed in 4% PFA overnight at 4◦C.
555 Slices were washed with PBS three times, 20 min each, and incubated in Streptavidin-Alexa
556 488 (S11223) or Alexa 647 (1:500, S32357, Invitrogen) and DAPI (1:1000, in 0.3% PBST)
557 overnight at 4°C. Slices were washed in 0.3% PBST four times and mounted on glass slides

558 with Mowiol® 4-88. Mcherry fluorescence in the MEC was examined with confocal imaging
559 and those animals where virus injection missed MEC L5 were excluded.

560 For staining of the interneuron marker parvalbumin (PV), slices were prepared as described
561 above, then incubated in primary antibody solution containing mouse anti-PV (1:1000, PV
562 235, Swant) and 5% NGS in 0.3% PBST for 48 hrs at 4°C. Slices were then washed and
563 incubated in secondary antibody solution with Alexa-conjugated Streptavidin and DAPI
564 prepared in 0.3% PBST and mounted on glass slides after overnight incubation.

565 A Zeiss LSM800 microscope was used for image acquisition of the slices. Pinhole was set to
566 1 Airy Unit. Objectives used include x10 (air), x20 (air) and x40 (oil) to image the
567 hippocampal formation, morphology of biocytin filled cells, and immunolabelling of
568 interneurons, respectively.

569 **Image processing and generation**

570 Experimental design sketches were generated using brainrender (Claudi et al., 2021) or
571 Affinity Designer. Where necessary images were cropped and size-adjusted using
572 Photoshop, Pixelmator and ImageJ softwares.

573 Statistics

574 Statistical tests (Student's t-test, Chi-squared test, Wilcoxon signed rank test) were
575 performed using R (www.r-project.org) 3.6.0, 4.0.0 and 4.0.3. Normality was tested for using
576 both the Shapiro-Wilk test and QQ plots. All data is presented in the format of mean ± SEM
577 unless otherwise stated. A p-value < 0.05 was regarded as significant.

578 Data availability

579 On publication data and analysis scripts will be made publicly available via University of
580 Edinburgh's Datashare service (http://datashare.is.ed.ac.uk/). This is an online data

repository maintained by the University. MAPseq data will be made available at NLM Sequence Read Archive BioProject.

Code availability

Analysis script will be made publicly available upon publication via University of Edinburgh's Datashare service

Acknowledgements

We thank Matt Nolan and Nolan Lab for discussions and sharing reagents and equipment. We thank Justus Kebschull for sharing his insight in MAPseq technique, Maria Doitsidou for sharing her equipment and lab space. We also thank Matt Nolan, Klara Gerlei, Brianna Vandrey, Christina Brown and our lab members for critical reading of the manuscript and Gamze Şener for her help with early experiments. C.M. was supported by a BBSRC project grant BB/M025454/1. This research was supported by a Royal Society and Wellcome Trust Sir Henry Dale fellowship 211236/Z/18/Z.

Contributions

S.Y.T. and M.Ö. equally contributed to the study.

G.S. conceptualised the study, acquired funding and administered the project. G.S. and S.Y.T. performed MAPseq experiments and analysed the data. M.Ö., G.S. and E.S. performed electrophysiology experiments and data analysis. Anatomy and histology experiments were performed and analysed by S.Y.T., G.S., M.Ö., E.S., and M.R.. C.M. developed reagents. Z.B. developed analysis tools and contributed to early discussions. G.S., S.Y.T., E.S. and M.Ö. prepared the original manuscript.

605 ## References

606 Arber, S., Ladle, D.R., Lin, J.H., Frank, E., and Jessell, T.M. (2000). ETS gene Er81 controls
607 the formation of functional connections between group Ia sensory afferents and motor
608 neurons. Cell *101*, 485–498.

609 Beed, P., de Filippo, R., Holman, C., Johenning, F.W., Leibold, C., Caputi, A., Monyer, H.,
610 and Schmitz, D. (2020). Layer 3 Pyramidal Cells in the Medial Entorhinal Cortex Orchestrate
611 Up-Down States and Entrain the Deep Layers Differentially. Cell Rep. *33*, 108470.

612 Cappaert, N.L.M., Van Strien, N.M., and Witter, M.P. (2015). Chapter 20 - Hippocampal
613 Formation. In The Rat Nervous System (Fourth Edition), G. Paxinos, ed. (San Diego:
614 Academic Press), pp. 511–573.

615 Claudi, F., Tyson, A.L., Petrucco, L., Margrie, T.W., Portugues, R., and Branco, T. (2021).
616 Visualizing anatomically registered data with brainrender. Elife *10*.
617
618 Colgin, L.L. (2016). Rhythms of the hippocampal network. Nature Reviews Neuroscience *17*,
619 239–249.

620 Czajkowski, R., Sugar, J., Zhang, S.-J., Couey, J.J., Ye, J., and Witter, M.P. (2013).
621 Superficially projecting principal neurons in layer V of medial entorhinal cortex in the rat
622 receive excitatory retrosplenial input. J. Neurosci. *33*, 15779–15792.

623 Dolorfo, C. L., and D. G. Amaral. 1998. Entorhinal Cortex of the Rat: Topographic
624 Organization of the Cells of Origin of the Perforant Path Projection to the Dentate Gyrus. The
625 Journal of Comparative Neurology 398 (1): 25–48.
626
627 Dudman, J.T., Tsay, D., and Siegelbaum, S.A. (2007). A role for synaptic inputs at distal
628 dendrites: instructive signals for hippocampal long-term plasticity. Neuron *56*, 866–879.

629 Frankland, P. W. & Bontempi, B. The organization of recent and remote memories. *Nat. Rev.*
630 *Neurosci.* **6**, 119–130 (2005).
631
632 Gerfen, C.R., Paletzki, R., and Heintz, N. (2013). GENSAT BAC cre-recombinase driver
633 lines to study the functional organization of cerebral cortical and basal ganglia circuits.
634 Neuron *80*, 1368–1383.

635 Kebschull, J.M., da Silva, P.G., Reid, A.P., Peikon, I.D., Albeanu, D.F., and Zador, A.M.
636 (2016). High-Throughput Mapping of Single-Neuron Projections by Sequencing of Barcoded
637 RNA. Neuron *91*, 975–987.

638 Ketz, N., Morkonda, S.G., and O'Reilly, R.C. (2013). Theta coordinated error-driven learning
639 in the hippocampus. PLoS Comput. Biol. *9*, e1003067.

640 Khodagholy, D., Gelinas, J.N., and Buzsáki, G. (2017). Learning-enhanced coupling
641 between ripple oscillations in association cortices and hippocampus. Science *358*, 369–372.

642 Kitamura, T., Pignatelli, M., Suh, J., Kohara, K., Yoshiki, A., Abe, K., and Tonegawa, S.
643 (2014). Island Cells Control Temporal Association Memory. Science *343*, 896–901.

644 Kitamura, T., Ogawa, S.K., Roy, D.S., Okuyama, T., Morrissey, M.D., Smith, L.M., Redondo,
645 R.L., and Tonegawa, S. (2017). Engrams and circuits crucial for systems consolidation of a
646 memory. Science *356*, 73–78.

Köhler, C. (1985). A projection from the deep layers of the entorhinal area to the hippocampal formation in the rat brain. Neurosci. Lett. *56*, 13–19.

Koster, R., Chadwick, M.J., Chen, Y., Berron, D., Banino, A., Düzel, E., Hassabis, D., and Kumaran, D. (2018). Big-Loop Recurrence within the Hippocampal System Supports Integration of Information across Episodes. Neuron *99*, 1342–1354.e6.

Kumaran, D., Hassabis, D., and McClelland, J.L. (2016). What Learning Systems do Intelligent Agents Need? Complementary Learning Systems Theory Updated. Trends Cogn. Sci. *20*, 512–534.

Marr, D. (1971). Simple memory: a theory for archicortex. Philos. Trans. R. Soc. Lond. B Biol. Sci. *262*, 23–81.

McClelland, J.L., McNaughton, B.L., and O'Reilly, R.C. (1995). Why there are complementary learning systems in the hippocampus and neocortex: insights from the successes and failures of connectionist models of learning and memory. Psychol. Rev. *102*, 419.

McClure, C., Cole, K.L.H., Wulff, P., Klugmann, M., and Murray, A.J. (2011). Production and titering of recombinant adeno-associated viral vectors. J. Vis. Exp. e3348.

Murray, A.J., Sauer, J.-F., Riedel, G., McClure, C., Ansel, L., Cheyne, L., Bartos, M., Wisden, W., and Wulff, P. (2011). Parvalbumin-positive CA1 interneurons are required for spatial working but not for reference memory. Nat. Neurosci. *14*, 297–299.

Naber, P.A., Lopes da Silva, F.H., and Witter, M.P. (2001). Reciprocal connections between the entorhinal cortex and hippocampal fields CA1 and the subiculum are in register with the projections from CA1 to the subiculum. Hippocampus *11*, 99–104.

Ognjanovski, N., Schaeffer, S., Wu, J., Mofakham, S., Maruyama, D., Zochowski, M., and Aton, S.J. (2017). Parvalbumin-expressing interneurons coordinate hippocampal network dynamics required for memory consolidation. Nat. Commun. *8*, 15039.

Pastoll, H., White, M., and Nolan, M. (2012). Preparation of parasagittal slices for the investigation of dorsal-ventral organization of the rodent medial entorhinal cortex. J. Vis. Exp.

Petreanu, L., Huber, D., Sobczyk, A., and Svoboda, K. (2007). Channelrhodopsin-2–assisted circuit mapping of long-range callosal projections. Nat. Neurosci. *10*, 663–668.

Rozov, A., Rannap, M., Lorenz, F., Nasretdinov, A., Draguhn, A., and Egorov, A.V. (2020). Processing of Hippocampal Network Activity in the Receiver Network of the Medial Entorhinal Cortex Layer V. The Journal of Neuroscience *40*, 8413–8425.

Ruth, R. E., Collier, T. J. & Routtenberg, A. Topography between the entorhinal cortex and the dentate septotemporal axis in rats: I. Medial and intermediate entorhinal projecting cells. J. Comp. Neurol. **209**, 69–78 (1982).

Schapiro, A.C., Turk-Browne, N.B., Botvinick, M.M., and Norman, K.A. (2017). Complementary learning systems within the hippocampus: a neural network modelling approach to reconciling episodic memory with statistical learning. Philos. Trans. R. Soc. Lond. B Biol. Sci. *372*.

Sürmeli, G., Marcu, D.C., McClure, C., Garden, D.L.F., Pastoll, H., and Nolan, M.F. (2015). Molecularly Defined Circuitry Reveals Input-Output Segregation in Deep Layers of the Medial Entorhinal Cortex. Neuron *88*, 1040–1053.

Squire, L. R., Genzel, L., Wixted, J. T. & Morris, R. G. Memory consolidation. Cold Spring Harb. Perspect. Biol. **7**, a021766 (2015).

Swanson, L.W., and Köhler, C. (1986). Anatomical evidence for direct projections from the entorhinal area to the entire cortical mantle in the rat. J. Neurosci. *6*, 3010–3023.

Tamamaki, N., and Nojyo, Y. (1995). Preservation of topography in the connections between the subiculum, field CA1, and the entorhinal cortex in rats. J. Comp. Neurol. *353*, 379–390.

Wang, Y., Kakizaki, T., Sakagami, H., Saito, K., Ebihara, S., Kato, M., Hirabayashi, M., Saito, Y., Furuya, N., and Yanagawa, Y. (2009). Fluorescent labeling of both GABAergic and glycinergic neurons in vesicular GABA transporter (VGAT)–Venus transgenic mouse. Neuroscience *164*, 1031–1043.

Witter, M.P., and Amaral, D.G. (1991). Entorhinal cortex of the monkey: V. Projections to the dentate gyrus, hippocampus, and subicular complex. J. Comp. Neurol. *307*, 437–459.

Witter, M.P., Doan, T.P., Jacobsen, B., Nilssen, E.S., and Ohara, S. (2017). Architecture of the Entorhinal Cortex A Review of Entorhinal Anatomy in Rodents with Some Comparative Notes. Front. Syst. Neurosci. *11*, 46.

Wozny, C., Beed, P., Nitzan, N., Pössnecker, Y., Rost, B.R., and Schmitz, D. (2018). VGLUT2 Functions as a Differential Marker for Hippocampal Output Neurons. Front. Cell. Neurosci. *12*, 337.

Figure supplements

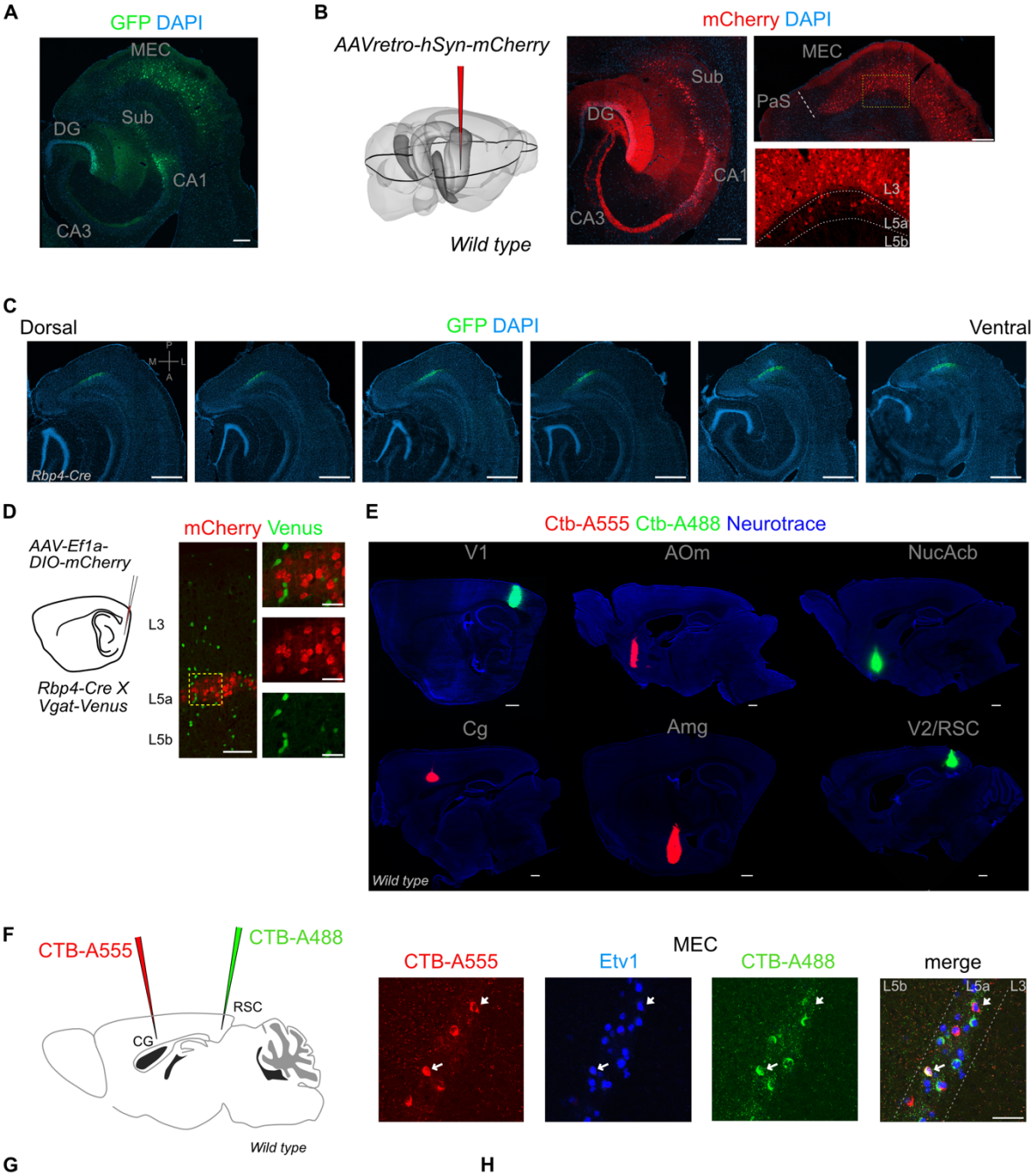

G

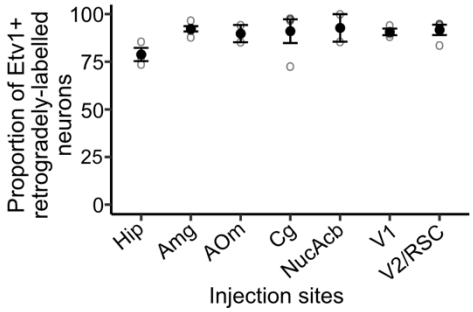

H

Target	n (mice)	Mean percentage	Total number of cells
Hip	3	78.8 ± 3.52	749
Amg	5	92.3 ± 1.41	943
AOm	2	89.8 ± 4.50	531
Cg	4	91.1 ± 6.19	527
NucAcb	2	92.8 ± 7.24	297
V1	3	90.7 ± 1.76	774
V2/RSC	4	91.8 ± 2.73	874

Figure 1, figure supplement 1. Injection site images, quantification of co-localisation between retrograde markers and Etv1.

A, Immunostained horizontal sections showing the injection site in the intermediate hippocampus of a retrograde AAV virus. L3 and L5a cells in the MEC were retrogradely-labelled via GFP expression driven by the CAG (CMV early enhancer/chicken β actin) promoter (Scale bar: 200 μm).
B, Results in (A) were replicated with an AAV virus that enables retrograde labelling of cells via expression of mCherry driven by the human synapsin (hSyn) promoter (Scale bar: 200 μm).
C, Immunostained brain sections in horizontal plane from a single brain showing the dorso-ventral spread of virus-mediated reporter gene expression in the Rbp4-Cre mice (Scale bar: 500 μm).
D, Schemmatic of a Cre-dependent mCherry expressing virus injection in the deep MEC of Rbp4-Cre X Vgat-Venus mouse line (left). Immunostained brain sections in the MEC showing absence of overlap between mCherry and Venus which marks GABAergic interneurons (right). Scale bar: 100 μm, Inset scale bar: 30 μm)
E, Immunostained brain sections in the sagittal plane showing injection sites of fluorophore-coupled CTB (Cholera toxin beta subunit; Scale bar: 500 μm).
F, Schematic of a two-colour retrograde dye injection in the cingulate and retrosplenial cortices of wild-type mice (left). Immunostaining in the MEC shows overlap between Etv1 expression and retrograde dyes (right; Scale bar: 50 μm)
G,H, Quantification of overlap between retrograde labelling from cortical target areas and Etv1 expression in L5a of the MEC. The number of mice, mean proportion and total cells counted for each area are shown in the table.

Hip, hippocampus; Amg, amygdala; AOm, medial anterior olfactory area; Cg, cingulate area; NucAcb, nucleus accumbens; V1, primary visual cortex; V2, secondary visual areas; RSC, retrosplenial cortex.

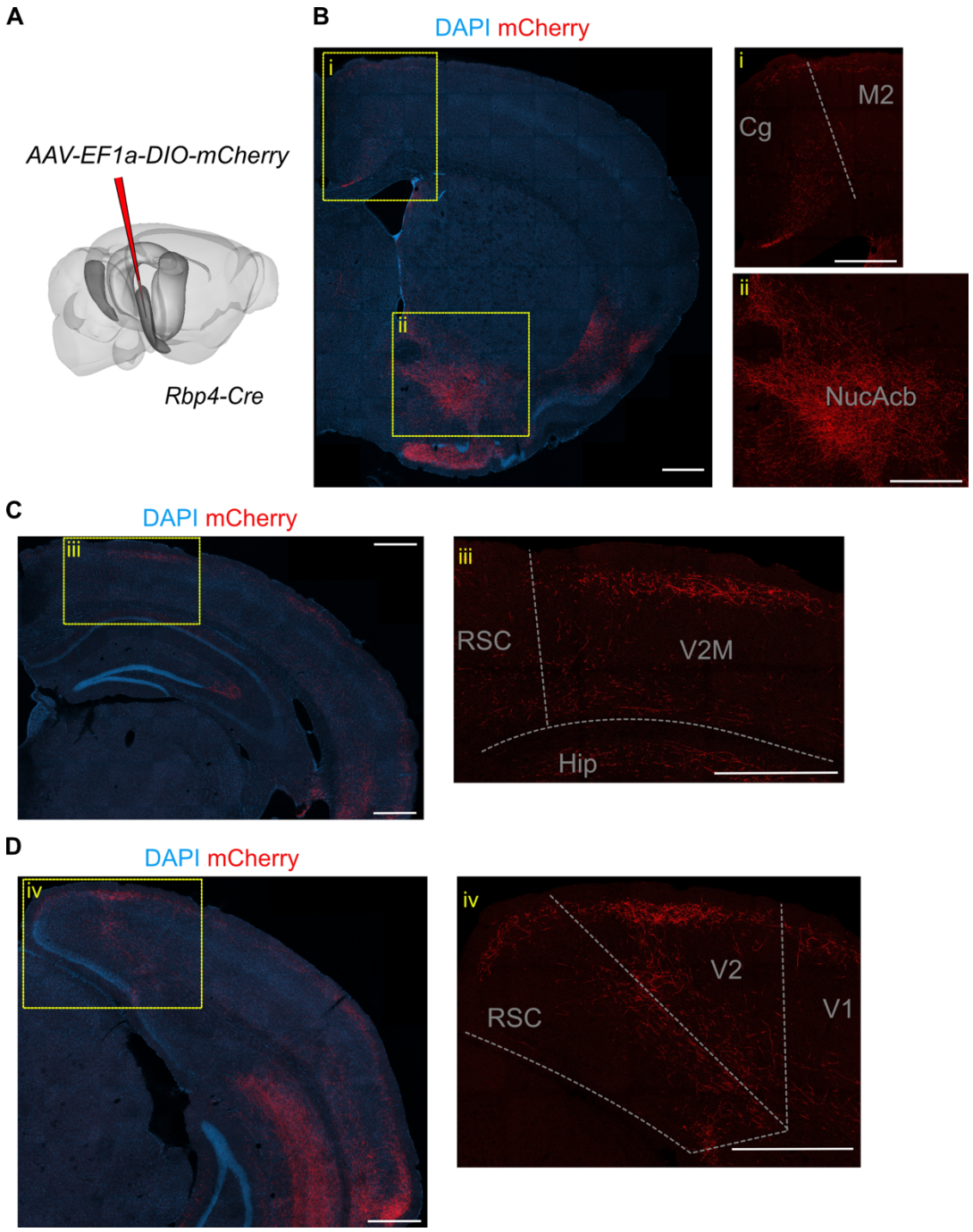

Figure 1, figure supplement 2. L5a neurons of the MEC innervate neocortical and subcortical areas.
A.Schematic showing the injection site of a Cre-dependent virus in the deep MEC of *Rbp4-Cre* mice.
B. Confocal image of a coronal brain slice showing axons originating from entorhinal L5a in the anterior telencephalon. Insets show higher magnification images of boxed areas.
C. Confocal image of a coronal brain slice showing axons originating from entorhinal L5a in the mid-telencephalon. Inset shows higher magnification image of boxed area.
D. Confocal image of a coronal brain slice showing axons originating from entorhinal L5a in the posterior telencephalon. Inset shows higher magnification image of boxed area.

Cg, cingulate area; M2, secondary motor area; V1, primary visual cortex; V2M, secondary visual area (medial); RSC, retrosplenial cortex; RSC, retrosplenial cortex; Hip, hippocampus; NucAcb, nucleus accumbens.

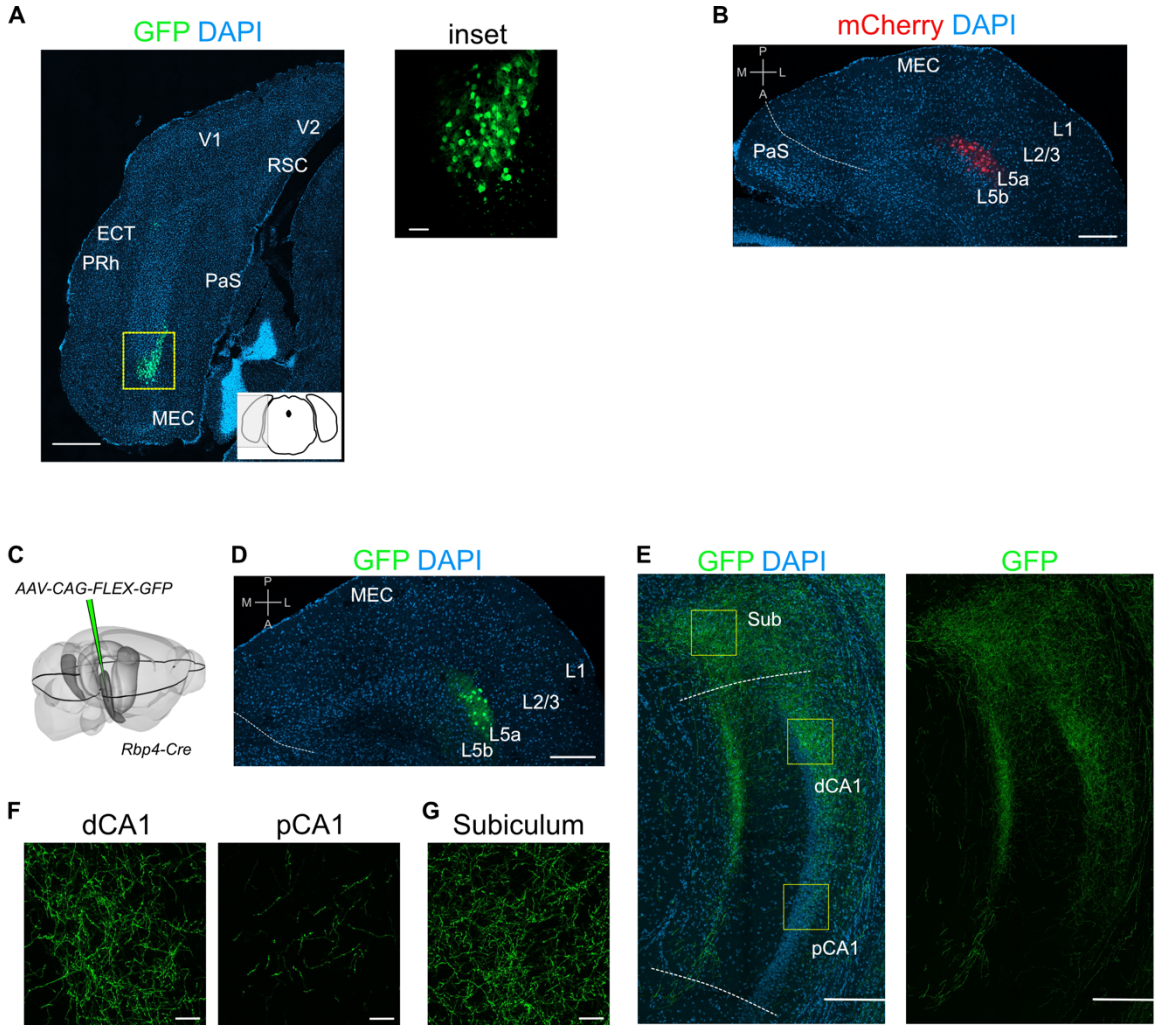

Figure 2, figure supplement 1. Injection site images and additional examples of axon labelling in CA1.
A, Immunostained brain section in the coronal plane showing cell body labelling at the injection site in MEC (Scale bar: 500 µm). Inset shows a higher magnification view of the boxed area (Scale bar: 50 µm). Schematic of a coronal brain section indicates the antero-posterior position of the section.
B, Immunostained brain section in the horizontal plane showing cell body labelling at the injection site in MEC (Scale bar: 200 µm).
C, Schematic showing the injection site of a Cre-dependent virus in the deep MEC of *Rbp4-Cre* mice. The black outline in the horizontal plane roughly corresponds to the dorso-ventral position of the slice shown in (D).
D, Immunostained brain section in the horizontal plane showing cell body labelling at the injection site in MEC (Scale bar: 200 µm).
E, Immunostained brain section in the horizontal plane showing the distribution of axons of MEC L5a cells in the subiculum (Sub), distal CA1 (dCA1) and proximal CA1 (pCA1) (Scale bar: 200 µm).
F, High-magnification images of the pyramidal cell layer in dCA1 and pCA1 showing axonal and synaptic labelling (Scale bar: 20 µm).
G, High-magnification image of the subiculum showing axonal labelling (Scale bar: 20 µm).

Prh, Perirhinal cortex; ECT, Ectorhinal cortex; V1, primary visual cortex; V2, secondary visual cortex; RSC, retrosplenial cortex; PaS, parasubiculum.

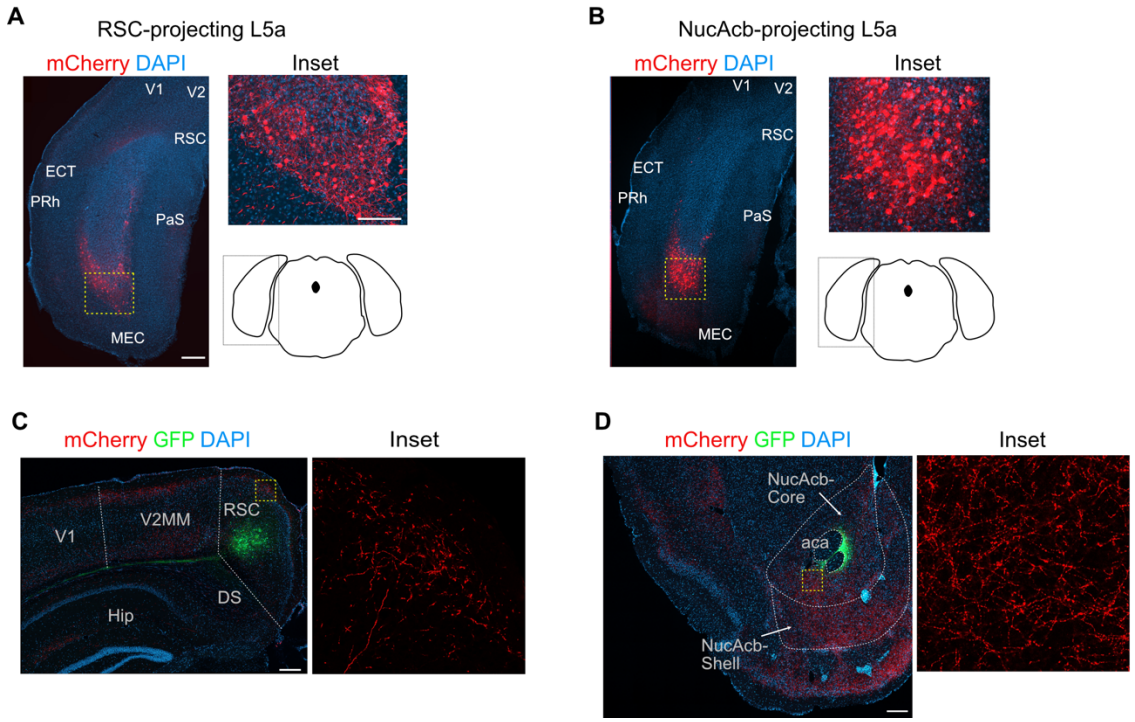

Figure 3, figure supplement 1. Combinatorial viral strategy effectively labels L5a cells of the MEC and their cortical projections.
A, B, Coronal brain sections showing labelled neurons in MEC with the combinatorial viral strategy (Scale bar: 500 µm). Inset: high-magnification confocal image of boxed region in left panel showing cell bodies in MEC expressing mCherry. Schematic of a coronal brain section indicates the antero-posterior position of the sections.
C, D, Coronal brain sections showing GFP expression and mCherry-labelled axon terminals at the injection sites in retrosplenial cortex (**D**) and nucleus accumbens (**E**) (Scale bar: 500 µm). Inset: high-magnification of boxed region in left panel.

RSC, retrosplenial cortex; NucAcb, nucleus accumbens; DS, dorsal subiculum; aca, anterior commissure anterior part; V2, secondary visual area medial part

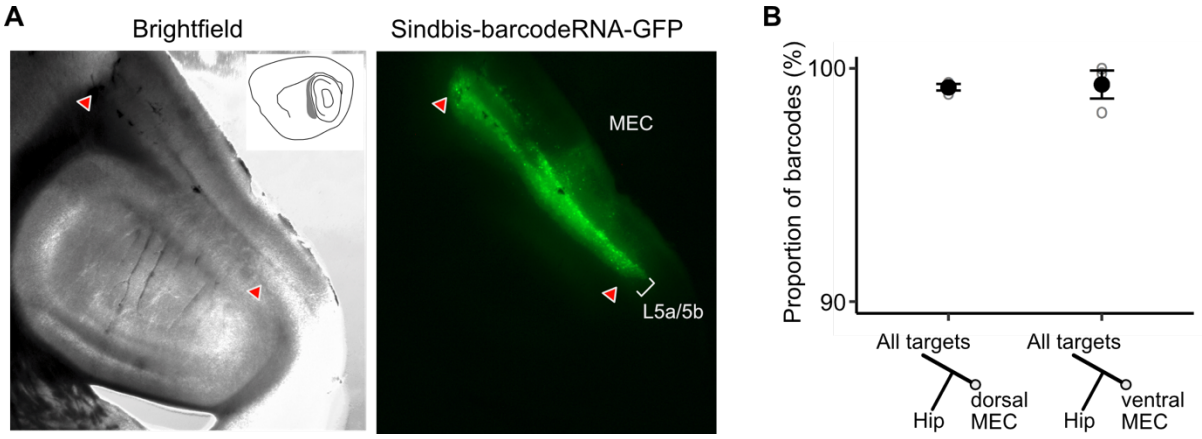

Figure 4, figure supplement 1. Verification of viral expression and further MAPseq data visualisation.
A, Brightfield and epifluorescence microscope images of the injection site on a sagittal brain section showing the spread of neurons infected by the MAPseq virus library in wild type mice.
B, A neuron's position in the dorso-ventral axis does not affect the likelihood of collateralisation of its axons to the hippocampus (Paired two-tailed Wilcoxon signed rank test, p = 0.75, median proportion of collateralizing barcodes in dEC = 98.4%, vEC = 98.9%, n = 3).

A

	SO (n = 18)	SP Pyr (n = 64)	SP FSint (n = 34)	SP NFSint (n = 15)	SR (n = 14)
Vm rest (mV)	-63 ± 1.48	-66.7 ± 0.6	-63.7 ± 0.7	-63.1 ± 0.9	-60.3 ± 1.3
IR (MΩ)	339 ± 64.1	146.9 ± 6.5	178.2 ± 29.4	214.1 ± 18.3	287.3 ± 48.7
Tm (ms)	22.3 ± 6.8	23.4 ± 2.1	14.7 ± 1.7	21.2 ± 3.7	25.2 ± 4.4
Rheobase (pA)	65.8 ± 17.8	112.8 ± 8.5	128.2 ± 15.1	83.9 ± 12.3	62.8 ± 8.8
Sag coefficient	0.85 ± 0.2	0.85 ± 0.01	0.86 ± 0.02	0.87 ± 0.01	0.85 ± 0.02

B

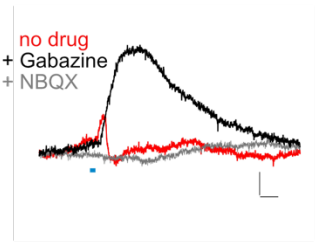

C

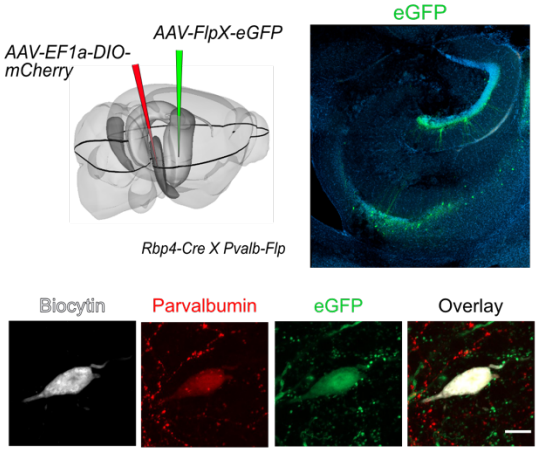

D

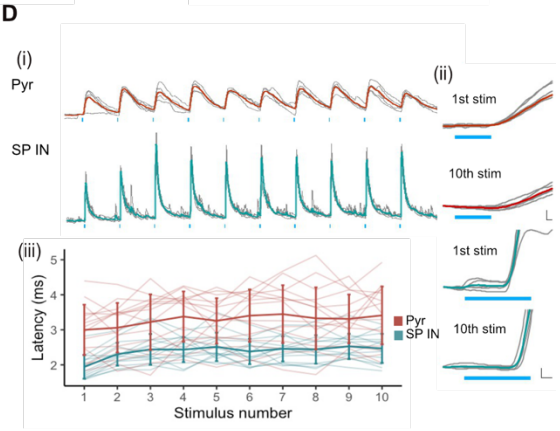

E

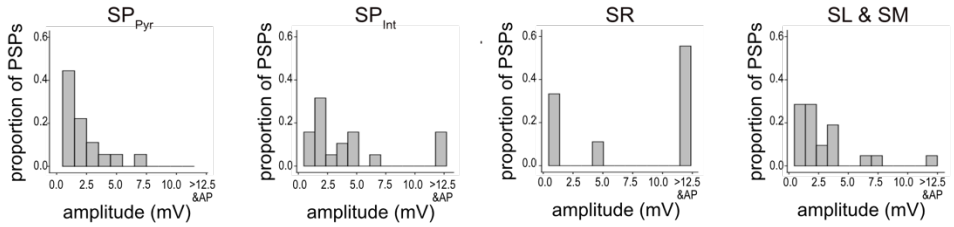

F

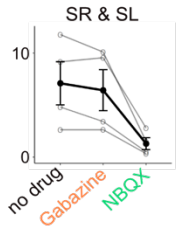

G

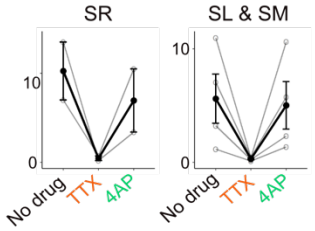

H

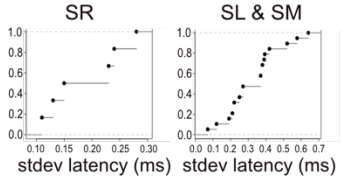

Figure 5, figure supplement 1. Experimental design and properties of responses to optogenetic stimulation of axons originating from L5a of the MEC.

A,Summary table for biophysical properties of neurons recorded in the study.

B, An example of a biphasic response recorded from a pyramidal neuron upon 3ms stimulation of axons of MEC L5a neurons in CA1. A late hyperpolarising (red) response was abolished by application of Gabazine to reveal a larger depolarising PSP (black) which was abolished by application of NBQX (grey) (Scale bar: 10 ms, 0.5 mV).

C, Experimental strategy for fluorescence guided patch-clamp recordings made from Parvalbumin expressing neurons. Left: A FlpX-dependent GFP expressing virus was injected in the hippocampus in *Rbp4-CreX Pvalb-Flp* mice. Right: Confocal image of horizontal slice showing labelled interneurons in the hippocampus. Bottom: An example fast-spiking interneuron marked as described in **c**, that showed depolarising PSP upon light stimulation. During recording, the neuron was filled with biocytin and later stained with Streptavidin and Anti-Parvalbumin antibody.

D, (i) Traces of responses to a train of 10 light stimulation (blue lines), showing relatively stable EPSP amplitude across simulations. (Scale bar: 30 ms, 1 mV) (ii) Magnified images of 1st and 10th pulse illustrate the invariant latency in one example cell (Scale bars: 0.5 ms, 0.5 mV) (iii) Quantification of latency across the train in all cells. Error bars represent SEM.

E, Plots showing the frequency distribution of PSP amplitudes in pyramidal neurons and interneurons. PSPs over 12.5 mV were detected in interneurons and often resulted in spiking responses. (SP_{Pyr} : n = 19, SP_{int} : n = 19, SR : n = 9, SL&SM : n = 22 cells).

F, Effects of bath application of Gabazine and NBQX on PSPs recorded from interneurons in SR and SL. The PSP amplitudes were largely unaffected by application of Gabazine (SR: n = 2 cells & SL n = 2 cells, p = 0.28, 2-tailed Student's t test) but were largely blocked by NBQX (SR: n = 2 cells & SL n = 2 cells, p = 0.04, 2-tailed Student's t test) indicating AMPA receptor mediated glutamatergic synaptic transmission.

G, Effects of bath application of TTX and 4-AP on the response amplitude PSPs recorded from interneurons in SR, SL and SM (SR: n = 2, SL: n = 3, SM: n = 1 cells).

H, Cumulative probability plots of standard deviation of latencies for neurons with PSP responses that were > 1 mV in amplitude. EPSPs of interneurons in all layers except SO had a short latency after light stimulation (mean latency SR: 2.00 ± 0.08 ms, n = 6 cells; SL & SM: 2.12 ± 0.21 ms, n = 23 cells). In SO 2 out of 3 of the evoked PSPs had a larger latency of onset (mean latency = 8.5 ± 0.63 ms, n = 2 cells, 2 mice, data not shown).